

Aerodynamics of biplane and tandem wings at low Reynolds numbers

R. Jones¹ · D. J. Cleaver¹ · I. Gursul¹

Received: 5 December 2014 / Revised: 21 April 2015 / Accepted: 20 May 2015
© Springer-Verlag Berlin Heidelberg 2015

Abstract Experiments were performed to investigate the aerodynamic characteristics of two-wing configurations at a low Reynolds number of 100,000. The wing models were rectangular flat plates with a semi-aspect ratio of two. The stagger between the wings was varied from $\Delta X/c = 0$ to 1.5; the gap was varied from $\Delta Y/c = 0$ to 2 and $\Delta Y/c = -1.5$ to 1.5 for biplane and tandem configurations, respectively, with the decalage angle fixed at 0° . Lift, drag, aerodynamic efficiency and power efficiency ratios show that for small incidence angles, performance compared with the single wing is degraded. However, for single-wing post-stall angles of attack, lift performance improves and stall is delayed significantly for many configurations with nonzero gap, i.e., $\Delta Y/c \geq 0$. For a fixed angle of attack, there are optimal gaps between the wings for which total lift becomes maximum. Particle image velocimetry measurements show that performance improvement relies heavily on the strength of the inter-wing flow and the interaction of the separated shear layers from the leading edge and trailing edge of the leading wing with the trailing wing. Unsteady forces are found to intensify for certain two-wing configurations. A switching between the stalled and unstalled states for the trailing wing as well as a switching between the merged and distinct wakes is shown to have high flow unsteadiness and large lift fluctuations.

List of symbols

b	Semi-span
c	Chord length

✉ I. Gursul
i.a.gursul@bath.ac.uk

¹ Department of Mechanical Engineering, University of Bath,
Bath BA2 7AY, UK

C_D	Time-averaged drag coefficient
C_{D1}	Time-averaged drag coefficient of wing 1
C_{D2}	Time-averaged drag coefficient of wing 2
C_{Dm}	Time-averaged monoplane drag coefficient
C_{Dt}	Time-averaged total drag coefficient, $(C_{D1} + C_{D2})/2$
C_L	Time-averaged lift coefficient
C_{L1}	Time-averaged lift coefficient of wing 1
C_{L2}	Time-averaged lift coefficient of wing 2
C_{Lm}	Time-averaged monoplane lift coefficient
C_{Lt}	Time-averaged total lift coefficient, $(C_{L1} + C_{L2})/2$
q	Dynamic pressure
R_{AE}	Time-averaged aerodynamic efficiency ratio, $(C_{Lm}/C_{Dm})/(C_{Lm}/C_{Dm})$
R_D	Time-averaged drag ratio, C_{D1}/C_{Dm}
Re	Reynolds number, $\rho U_\infty c/\mu$
R_L	Time-averaged lift ratio, C_{L1}/C_{Lm}
R_{PE}	Time-averaged power efficiency ratio, $(C_{L1}^{3/2}/C_{D1})/(C_{Lm}^{3/2}/C_{Dm})$
sAR	Semi-aspect ratio
U'	Streamwise velocity component
u'	Standard deviation of streamwise velocity
U_∞	Freestream velocity
V	Crosswise velocity component
v'	Standard deviation of crosswise velocity
X	Streamwise/longitudinal coordinate
Y	Crosswise/transverse coordinate
Z	Spanwise coordinate
α	Angle of attack
δ	Decalage
$\Delta X/c$	Stagger between the wings
$\Delta Y/c$	Gap between the wings
μ	Viscosity
ρ	Density
σ_{CLm}	Standard deviation of lift coefficient for monoplane wing

σ_{CL1}	Standard deviation of lift coefficient for wing 1
σ_{CL2}	Standard deviation of lift coefficient for wing 2
ω	Vorticity

1 Introduction

In recent decades, there has been buoyant interest in the design and development of unmanned aerial vehicles (UAVs) due to their potential for a wide variety of applications, both military and civil. With advances in the production and availability of miniature sensors, video cameras and control hardware yielding a payload mass <18 g, UAVs with wing spans <15 cm weighing 100 to 200 g, referred to as micro-air vehicles (MAVs), are now possible. With the development of small electronic sensing devices, they also offer an excellent solution to the chemical, biological, radiological and nuclear threats (Mueller and DeLaurier 2001, 2003).

To be practicable, MAVs would be required to fly for 20 min to 2 h at a speed of around 50 km/h (14 ms^{-1}) requiring high power efficiency and lift-to-drag ratio, $C_L^{3/2}/C_D$ and L/D, respectively, in all weather conditions, i.e., precipitation, wind shear and gusts (Pelletier and Mueller 2000). Root-chord Reynolds numbers for MAVs range from 2×10^4 to 2×10^5 which puts them in a low Reynolds number regime far from conventional aircraft. Pelletier and Mueller (2000) have reported experimental results performed at low Reynolds numbers for thin flat and cambered plates with semi-aspect ratios ranging from 0.5 to 3. Their findings show that reducing the Reynolds number results in deteriorating wing performance which was indicated by large reductions in maximum L/D and $C_L^{3/2}/C_D$ values. Even for two-dimensional airfoils, Carmichael (1981) and Selig et al. (1989) showed that aerodynamic performance at low Reynolds numbers is degraded due to the formation of a laminar separation bubble.

Cleaver et al. (2011) postulated that fixed-wing MAVs would need to fly at relatively high angles of attack, close to stall conditions, in order to compensate for the inherent poor lift generation. This is a result of the characteristics of the flight speed, wing area and lift coefficient for a given weight/payload. Low flight speeds may be preferable for optical surveillance as well as for the controllability of the MAV (Null and Shkarayev 2005). Required lift coefficients up to 0.8 were suggested for MAVs (Torres and Mueller 2000; Davis et al. 1996). Of course, efforts to increase the payload, while highly desirable, will result in flying at even higher lift coefficients. Hence, post-stall flight would be inevitable during high angle of attack maneuvers and vertical gusts. These regimes of flight are associated with a number of detrimental phenomena. For example, Zaman et al. (1989) reported an unusually low-frequency

large-amplitude flow oscillation over an airfoil at low Reynolds numbers at the onset of static stall. The Strouhal number of the oscillation was an order of magnitude lower than the usual ‘bluff-body shedding’ which typically occurs during deep stall. The phenomenon was attributed to a periodic switching between stalled and unstalled states resulting in large lift fluctuations. This low-frequency oscillation as well as the well-known bluff-body Kármán vortex shedding typical for high angles of attack could be detrimental for MAV flight. Hence, delaying stall and improving performance at large incidence angles are crucial for MAV flight and stability. In the present investigation, two-wing configurations are proposed as a means of generating the required lift in the required volume while also delaying stall. These configurations include both biplane and tandem wings with a wide range of separations.

Early development of fixed-wing aircraft initially led to the prominence of biplane configurations. Theoretical predictions for two-wing configurations were considered by Prandtl and Tietjens (1957) which extends the lifting line theory to biplanes taking into consideration the relative stagger, gap and wing planform area. For an un-staggered biplane configuration, the theory predicts contributions of mutual induced drag from the interference of the free trailing vortices of the two lifting lines. In the case of a staggered biplane, however, it is shown that the aft wing reduces the induced drag of the fore wing and the fore wing increases the induced drag of the aft wing via their mutual interaction. The total induced drag of a biplane is shown to be smaller than that of a monoplane of the same span for the same total lift.

Knight and Noyes (1929a, b, c) were among the first researchers to publish experimental data on separate wing models in closely coupled two-wing configurations at a Reynolds number of approximately 150,000. It was found that the normal force coefficient of the lower wing and of the whole configuration exceeded the monoplane value for most variations in stagger and exhibited a higher stall angle. The total normal force coefficient was enhanced most when the stagger was large in the post-stall regime. Olson and Selberg (1976) investigated biplane configurations experimentally with a view to improving aircraft efficiency at Reynolds numbers based on wing chord of 2.9×10^5 to 4.7×10^5 . They found a substantial reduction in drag coefficient with respect to the monoplane over a wide range of angles of attack for most biplane configurations. Lift-to-drag ratios were noted to significantly increase over a wide range of lift coefficients compared with the monoplane as well as improvements in $C_L^{3/2}/C_D$ values. Moschetta and Thipyopas (2007) performed wind tunnel experiments at low Reynolds numbers ($Re = 66,000$) comparing the performance of a biplane MAV to a monoplane MAV with various wing planforms. Their experimental results and

theoretical predictions demonstrated that for a given flight condition, biplane MAV configurations can drastically increase the overall aerodynamic efficiency over the classical monoplane fixed-wing concept. They also concluded that for a given lift force, the biplane's induced drag force was lower than the monoplane. Traub (2001) tested biplane configurations with slender delta wings at a Reynolds number of 7.7×10^5 . It was found that gap without any stagger caused a lift reduction. Experiments and theoretical modelling revealed that lift is strongly affected by the gap but not so much by the stagger.

In the case of infinite aspect ratio wings, Scharpf and Mueller (1992) investigated experimentally tandem Wortmann FX63-137 airfoils at low Reynolds numbers. The downwash from the upstream airfoil was noted to be the most significant factor in altering the performance of the downstream airfoil at $Re = 2 \times 10^5$. This helped to maintain attached flow and delayed stall, resulting in drag reduction. The lift of the downstream airfoil degraded, but the total drag decreased and total lift increased, resulting in significant increase in the lift-to-drag ratio for certain configurations. This study shows that, even in the absence of trailing tip vortices, favorable aerodynamic effects are possible due to the wake interactions.

It is clear that MAV performance could benefit greatly from the utilization of two-wing configurations, and although there is a moderate amount of force coefficient data from which to draw conclusions, there is a clear deficit in understanding the flow physics and flow interactions by means of flow visualization and quantifiable flow field analysis. In the following sections, lift and drag coefficient data are presented for two-wing configurations in which gap and stagger are systematically varied. Lift, drag, aerodynamic efficiency and power efficiency coefficients of two-wing configurations are compared directly with single-wing values. Selected particle image velocimetry (PIV) measurements showing time-averaged flow field velocity magnitude, vorticity and velocity standard deviation (SD) are presented revealing new insight into the aerodynamic behavior. The main objective is to understand biplane and tandem wing interference effects at low Reynolds numbers with a view to improving MAV performance. Initially, the single wing is characterized after which biplane and tandem wing configurations are considered. Finally, the unsteady aerodynamic behavior of selected two-wing configurations is considered.

2 Experimental techniques

Experiments were performed in a low-speed, low-turbulence return-circuit open-jet wind tunnel at the University of Bath, Mechanical Engineering Department. The working

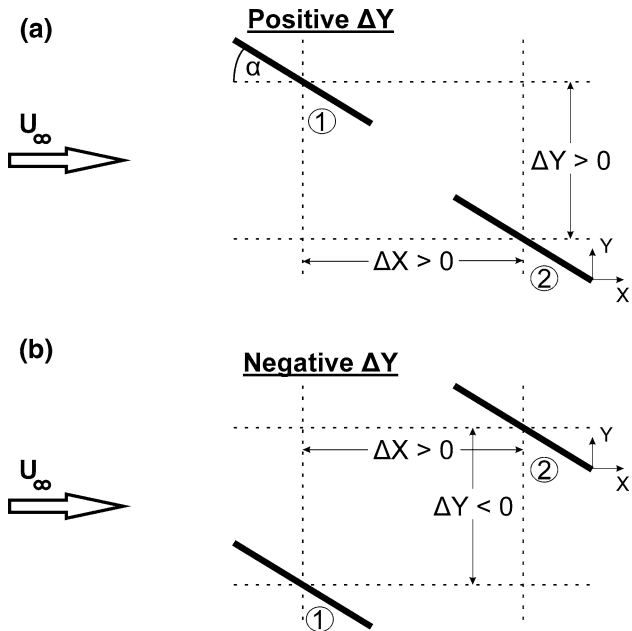


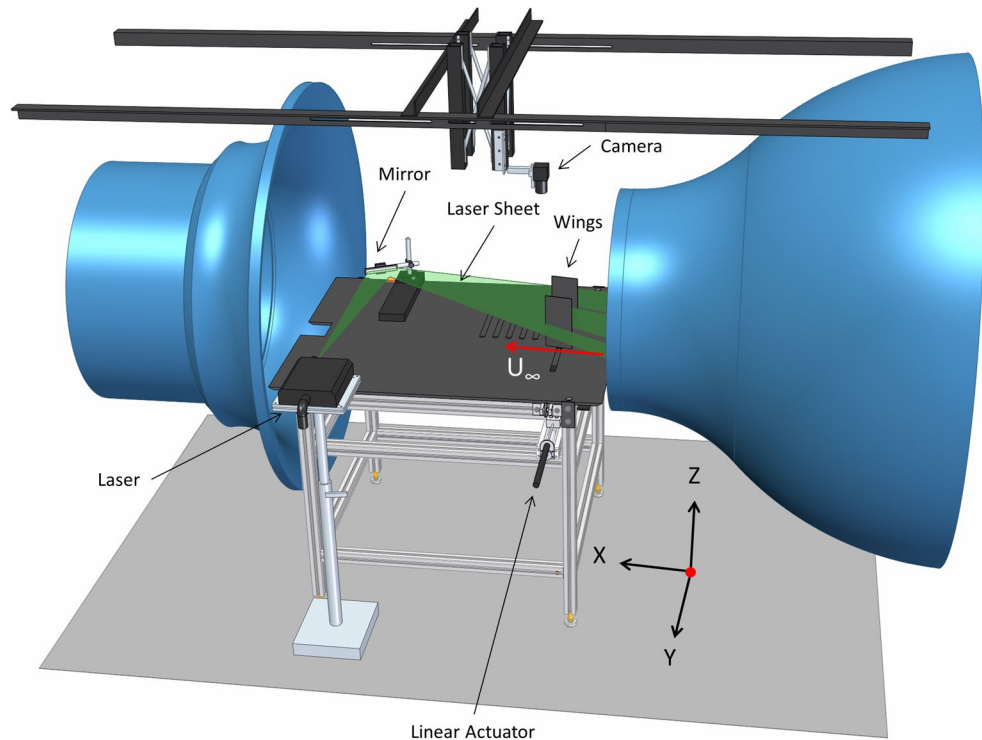
Fig. 1 Sign convention for the two-wing configurations; ΔX and ΔY are measured from the mid-chord locations

section of the wind tunnel had a circular nozzle diameter of 760 mm and a collector 1.1 m downstream. Previous work has determined the turbulence intensity to be 0.1 % at a maximum freestream velocity of 30 ms^{-1} (Wang and Gursul 2012). Experiments were performed at a freestream velocity of 15 ms^{-1} and Reynolds number of 100,000 with two-wing biplane and tandem configurations considering variable gap, stagger and angle of attack. Decalage angle was not varied and was fixed at $\delta = 0^\circ$. Four stagger values were considered, $\Delta X/c = 0, 0.5, 1$ and 1.5 . The gap was varied at regular intervals in the range $\Delta Y/c = 0$ to 2 and -1.5 to 1.5 for the biplane and tandem cases, respectively. Figure 1 illustrates the geometric parameterization convention in a cross-sectional plane of the two-wing configuration. The gap $\Delta Y/c$ is the position of the leading/upper wing with respect to the trailing/lower wing. In the case of tandem wing configurations, $\Delta Y/c$ is positive when the leading wing is above the trailing wing and negative when situated below. The angle of attack ranged from 5° to 30° at 5° intervals.

2.1 Experimental setup

Cantilever wing models of 200 mm semi-span and 100 mm chord length ($sAR = 2$) were fabricated from mild steel for the flat-plate rectangular wings studied. This aspect ratio was chosen as a representative case for MAV applications. In another study, we investigated the effect of wing flexibility for the same aspect ratio (Jones et al. 2015). In this study, the wings had square edges and a thickness of 2.5 %

Fig. 2 Wind tunnel experimental setup



chord and were inflexible in both spanwise and chordwise directions. The wing was separated from the force balance by an acrylic endplate mounted on top of the rig frame (see Fig. 2). The wing sting protruded through lipped slots in the endplate, aligned in the crosswise direction into which metal plates could be inserted to surround the wing sting thus providing a smooth continuous surface.

Figure 2 shows the test rig in situ with the PIV equipment also illustrated. The test rig used standard HepcoMotion® parts combined with bespoke components fabricated at the Department of Mechanical Engineering, University of Bath. The wing models were traversable across the endplate slots in the Y direction using linear actuators with a 200-mm stroke length, allowing continuous variation of $\Delta Y/c$, and had linear variable differential transformers (LVDTs) mounted at the ends yielding accurate position measurement. LVDTs were mounted to both of the linear actuators with the extension rods attached to the force balance carriages. The voltage signals were amplified using a Wheatstone bridge. The signals were sampled at 1 kHz through a LABVIEW® 7.1 program with the average of the last 1000 samples used to determine the wing positions relative to a set initial reference point. Linear position–voltage calibration curves, allowing the conversion from voltage to millimeters, were measured for both LVDTs at regular intervals to ensure accuracy. The typical $1 - R^2$ values of the position calibration curve regression statistics were $<10^{-4}$. The uncertainty in position for an individual LVDT was $<0.2\%$ of the maximum stroke length.

2.2 Force measurements

The wing models were connected to a pair of two-component aluminum binocular strain gauge force balances similar to Frampton et al. (2001). The forces in both the X and Y directions were measured by amplification of the signal from the strain gauges bonded to the points of largest strain. The strain gauges were configured in full Wheatstone bridge circuits with an excitation voltage of 5 V. The voltage signals were then processed through instrumentation amplifier circuits, converted by a 12-bit analog-to-digital converter and sampled at 1 kHz for 10,000 samples from each of the four output signals (lift and drag components for two wings). These signals were recorded using LABVIEW® 7.1 and post-processed in MATLAB®. The time average voltage was converted into time average force through force–voltage calibration curves obtained by applying fixed weights through a light cord passed over a low friction pulley attached to the edge of the rig converting the vertical force into a horizontal one as demonstrated by Mueller (2000). These calibration curves were obtained weekly, with a minimum of ten data points spread over discrete intervals from 0 N to 5 N, to ensure accuracy and that calibration coefficients did not change with time. The typical $1 - R^2$ values of the force calibration curve regression statistics were less than 10^{-5} .

The uncertainty of the force calibration coefficients was typically of the order 0.5 %. The uncertainty of the dynamic pressure q measured inside the nozzle was estimated to be

<3 %. The wings' chord and span had a machining tolerance of 0.1 and 0.05 %, respectively. These uncertainties were then combined using the random error analysis demonstrated by Moffat (1985). Force coefficient uncertainties were typically of the order of 3 % and less than the data point symbol sizes presented in this work. The uncertainty in angle of attack was estimated to be <0.3°.

2.3 Particle image velocimetry measurements

The wind tunnel was seeded with olive oil droplets, with a typical mean droplet size of 1 μm, produced by a six-jet TSI® oil droplet generator 9307-6. The measurement plane of interest was illuminated using a New Wave™ Solo III-15 Hz Nd:YAG double pulse dual laser-head system which had an energy output of 50 mJ per pulse at 15 Hz with a wavelength of 532 nm. The beam was passed through a cylindrical lens with a focal length of -15 mm and then focused through a spherical lens with a 1-m focal length. The laser was initially targeted across the wind tunnel freestream and reflected upstream toward the region of interest by a custom cut ion-plated silver mirror 140 mm × 15 mm × 3 mm with a 98 % reflective efficiency rating provided by Comar Optics Ltd. The PIV measurement plane of interest was parallel to the endplate surface at the mid-span ($Z/b = \frac{1}{2}$). Experiments have been performed at other spanwise planes in another study (Jones et al. 2015), and the effect of spanwise location was found to be insignificant except very close to the tip (5–10 % of the span). Therefore, in the interests of conciseness, we will only present data for the mid-span location.

All surfaces in the field of view were spray-painted black and sanded smooth multiple times to give the surfaces a smooth and uniform black finish so as to minimize anomalous artefacts in the PIV data. The majority of particle flow images were captured using a high frame rate TSI® PowerView™ Plus 4 mega-pixel camera mounted on a rigid steel frame suspended vertically above the experimental apparatus (see Fig. 2); the remainder were acquired using a 2 mega-pixel version of the same camera. In both cases, the camera lens was a Nikon 28 mm f/2.8D AF Micro-NIKKOR. The camera frame capture times and laser pulses were synchronized using a TSI® LaserPulse synchroniser. In all PIV experiments, the time difference between each of the frame pairs was fine-tuned for the individual experiment to obtain the best results but was of the order of 10 μs. For each wing configuration, 200 image pairs were captured. Image pairs were then analyzed using TSI's® Insight3G commercial software with a fast Fourier transform cross-correlation algorithm. For the 4 MP camera, an interrogation window size of 32 pixels × 32 pixels was used to determine velocity vectors of the flow in the plane of interest; for the 2 MP camera, an interrogation window size of 32 pixels × 32 pixels was used.

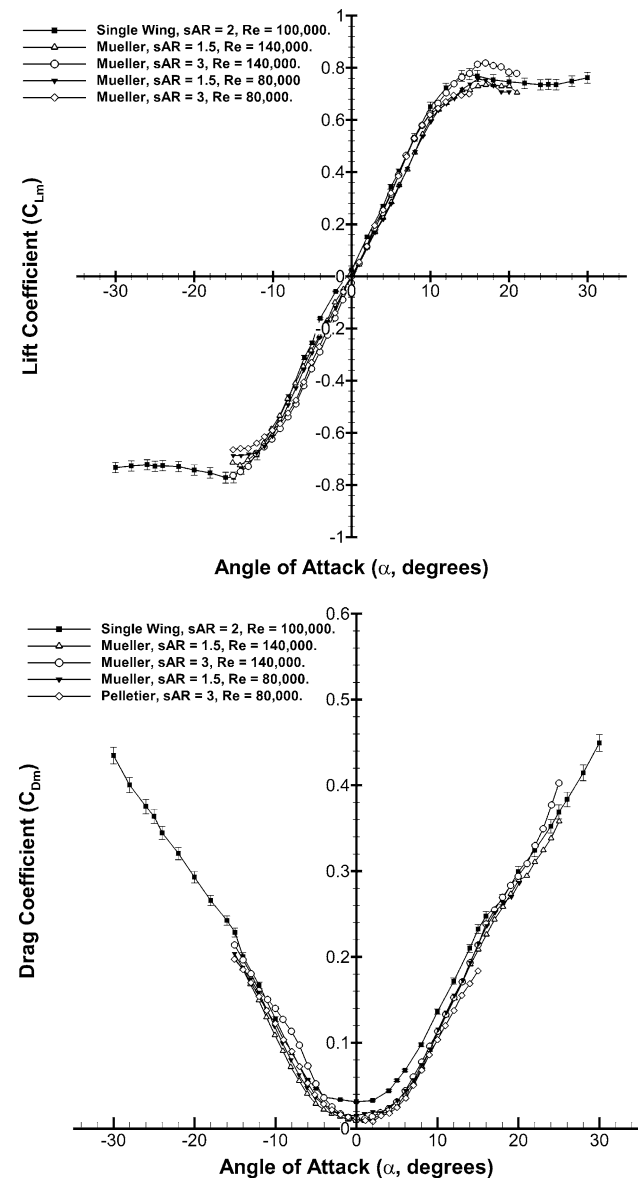


Fig. 3 Lift and drag coefficients for the single wing (flat plate, sAR = 2) at $Re = 100,000$. Measurements are compared with Mueller (2000), and Pelletier and Mueller (2000)

was used to determine velocity vectors of the flow in the plane of interest; for the 2 MP camera, an interrogation window size of 32 pixels × 32 pixels was used.

The thickness of the PIV laser sheet was 2 to 3 mm in the region of interest. The error in alignment of the laser sheet to the measurement plane was estimated to be of the order of 1 mm. The error in the calibration length scale was estimated to be typically of the order of 0.1 %. Errors due to the digitisation of the measured signal by data acquisition hardware were not considered significant.

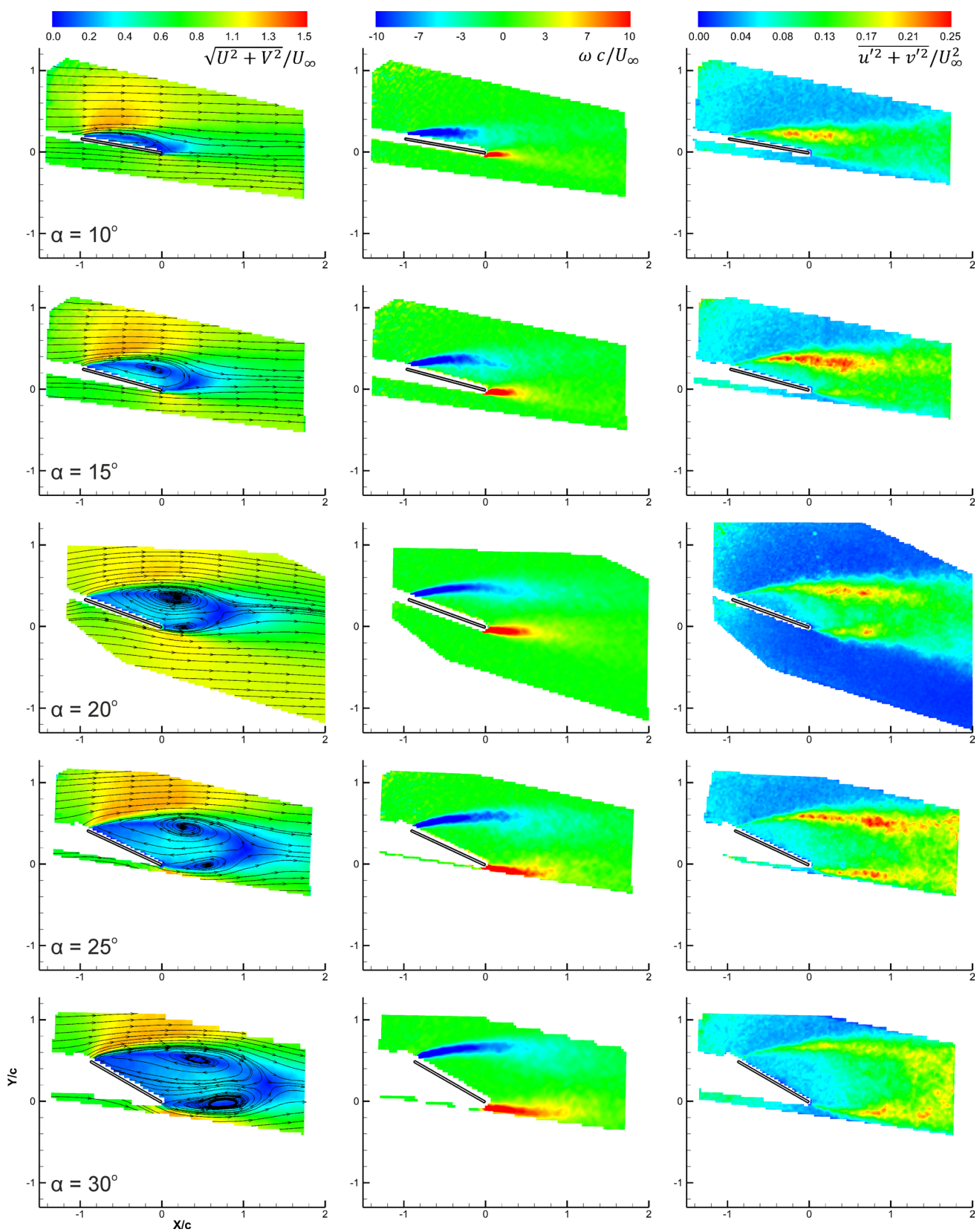


Fig. 4 Velocity magnitude and streamlines (*left*), vorticity (*center*) and standard deviation of velocity squared (*right*) at different angles of attack for the single wing

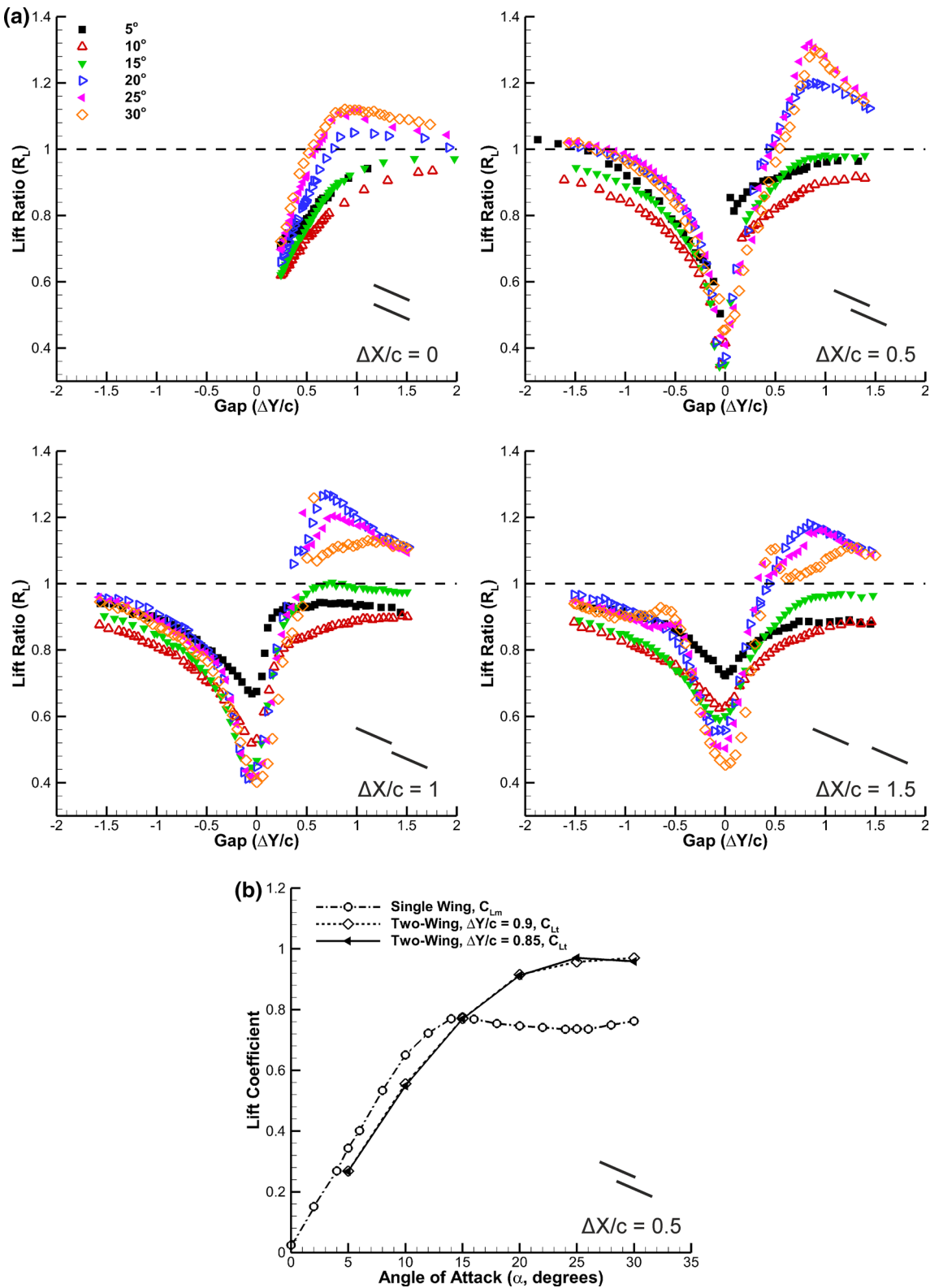


Fig. 5 **a** Total lift coefficient for two-wing configurations normalized by the lift coefficient of the single wing. Lift ratio above unity (dashed line) indicates greater lift compared with the single wing.

b Lift coefficient versus angle of attack for the single wing and two-wing cases with the highest stall angles

3 Results and discussion

Section 3.1 will discuss force and PIV measurements for the single wing and make comparisons with the results of (Mueller et al. 2000; Pelletier and Mueller 2000). Section 3.2 shall discuss lift, drag, aerodynamic efficiency and power efficiency ratios for two-wing configurations. The total lift and drag coefficients for two wings is defined as:

$$C_{Lt} = \frac{S_1 C_{L1} + S_2 C_{L2}}{S_1 + S_2} \quad \text{and} \quad C_{Dt} = \frac{S_1 C_{D1} + S_2 C_{D2}}{S_1 + S_2},$$

where C_{Lt} and C_{Dt} are the total lift and drag coefficients based on total planform area ($S_1 + S_2$) and C_{L1} , C_{L2} , C_{D1} and C_{D2} are the lift and drag coefficients of the separate wings (Traub 2001). In this study, $S_1 = S_2$ and hence these equations reduce to simply $C_{Lt} = (C_{L1} + C_{L2})/2$ and $C_{Dt} = (C_{D1} + C_{D2})/2$. In Sect. 3.3, the cause of the change

in performance is demonstrated through time-averaged PIV with corresponding lift coefficient measurements (C_{L1} , C_{L2} and C_{Dt}). Finally, Sect. 3.4 will discuss unsteady behavior.

3.1 Single wing

Figure 3 presents time-averaged lift and drag coefficient for the single wing with $sAR = 2$ at $Re = 10^5$. Force coefficient data taken from (Mueller et al. 2000; Pelletier and Mueller 2000) for flat plates with $sAR = 1.5$ and 3 at low Reynolds numbers $Re = 8 \times 10^4$ to 1.4×10^5 are also presented for comparison and validation. The current measurements are in good agreement. The maximum lift coefficient is $C_{Lm} = 0.77 \pm 0.02$, and stall angle is $\alpha_{stall} = 15^\circ$. The minimum drag coefficient was found at $\alpha = 0^\circ$ to be $C_{Dm} = 0.031 \pm 0.001$ which is greater than the findings of Mueller et al., and it is surmised that this is likely due to the

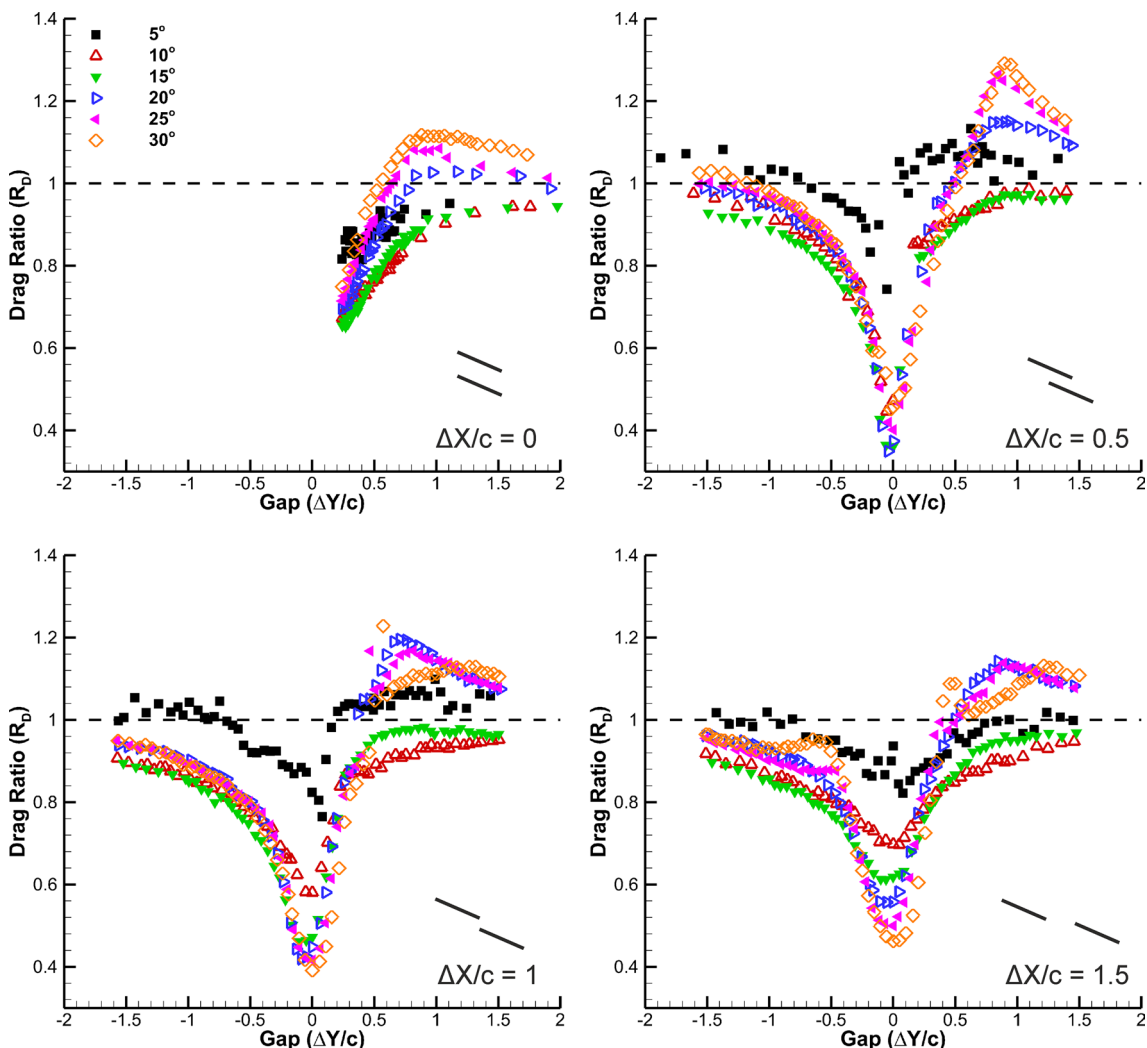


Fig. 6 Total drag coefficient for two-wing configurations normalized by the drag coefficient of the single wing. Drag ratio below unity (dashed line) indicates lower drag compared with the single wing

difference in leading- and trailing-edge geometry. In this work, wing models had square leading and trailing edges, whereas wing models used by Mueller et al. had elliptical leading edges and either tapered or elliptical trailing edges. It is likely that the square leading edge promotes boundary layer tripping thus producing a greater drag profile at $\alpha = 0^\circ$. It is unlikely that the difference in Reynolds number between the present data and Mueller et al.'s data contributes since the variations in the Reynolds number in their data do not affect the minimum drag. The gradient of the linear region is 3.48 rad^{-1} . Comparing with the lifting line for a finite wing of aspect ratio AR , as demonstrated by Pelletier and Mueller (2000):

$$a = \frac{a_0}{1 + \frac{1+\tau}{\pi AR} a_0}$$

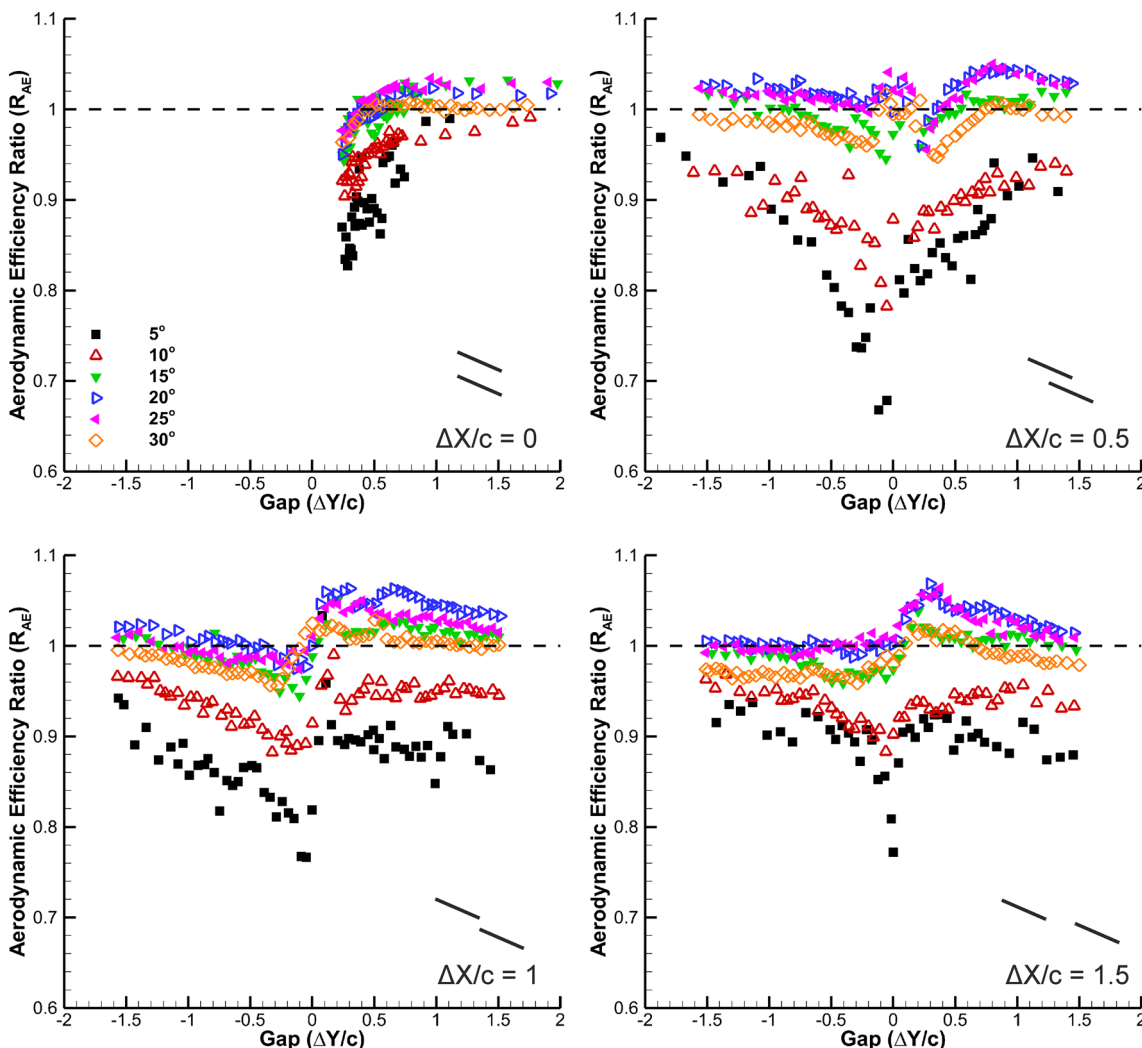


Fig. 7 Ratio of aerodynamic efficiency of two-wing configurations to that of the single wing. Data points above unity (*dashed line*) indicate greater aerodynamic efficiency compared with the single wing

Here, $AR = 4$, a_0 is taken as 2π and according to Glauert (1959) $\tau = 0.12$, which gives a gradient of 4.02. Considering the assumed value of a_0 , this agrees reasonably well with the measured value.

Shown in Fig. 4 are measurements of the single-wing flow field in the form of velocity magnitude with streamlines as well as vorticity and velocity SD squared. Flow separation clearly occurs for $\alpha \geq 10^\circ$ with clockwise recirculation flow emanating from the leading edge as a leading-edge shear layer. For $\alpha \geq 20^\circ$, in the time-averaged flow, there is also counterclockwise recirculation flow due to the trailing-edge shear layer that increases in size as the angle of attack is increased. The SD squared contour plots indicate relatively consistent levels of maximum turbulent energy for all incidence angles; however, the spread appears to increase with α .

3.2 Two-wing force measurements

3.2.1 Biplane configuration

Figures 5 and 6 present the ratios of total lift and drag coefficients to those of the single wing: $R_L = C_{Lr}/C_{Lm}$ and $R_D = C_{Dr}/C_{Dm}$. These are for stagger values of $\Delta X/c = 0, 0.5, 1$ and 1.5 in which the angle of incidence varies from $\alpha = 5^\circ$ to 30° . Figures 7 and 8 present the aerodynamic and power efficiency ratios, respectively. In all of the figures, the dashed line at $R = 1$ represents the single-wing value.

Starting with the biplane ($\Delta X/c = 0$) configuration, lift and drag ratios follow similar trends to one another. This is a result of mostly separated flows over the flat-plate wing. At small gaps ($\Delta Y/c$), lift and drag ratios are less than unity. As $\Delta Y/c$ increases, lift and drag ratios for angles of attack greater than or equal to 20° increase, exceeding the

single-wing value at approximately $\Delta Y/c = 0.6$, until $\Delta Y/c$ reaches 1.0 after which lift and drag ratios asymptote down to $R = 1$. The maximum lift ratios achieved in the vicinity of $\Delta Y/c = 1$ for $\alpha = 25^\circ$ and 30° are comparably similar, whereas the drag ratio continue to increase from 25° to 30° . The maximum lift and drag ratio was $R_L = 1.12 \pm 0.03$ and $R_D = 1.12 \pm 0.03$, respectively, and was achieved at 30° and $\Delta Y/c = 0.88$. For angles of attack 15° or less, lift and drag ratios tend asymptotically toward $R_{L,D} = 1$ as $\Delta Y/c$ increases. The lift ratio also reveals that the lift continues to increase beyond the stall angle of the single wing ($\alpha_{stall} = 15^\circ$ after which the lift coefficient of the single wing remains approximately constant up to $\alpha = 30^\circ$, see Fig. 3) and stall is significantly delayed (up to 30°) for some values of $\Delta Y/c$.

In terms of the aerodynamic efficiency ratio [$R_{AE} = (C_{Lr}/C_{Dr})/(C_{Lm}/C_{Dm})$] for $\Delta X/c = 0$, at small

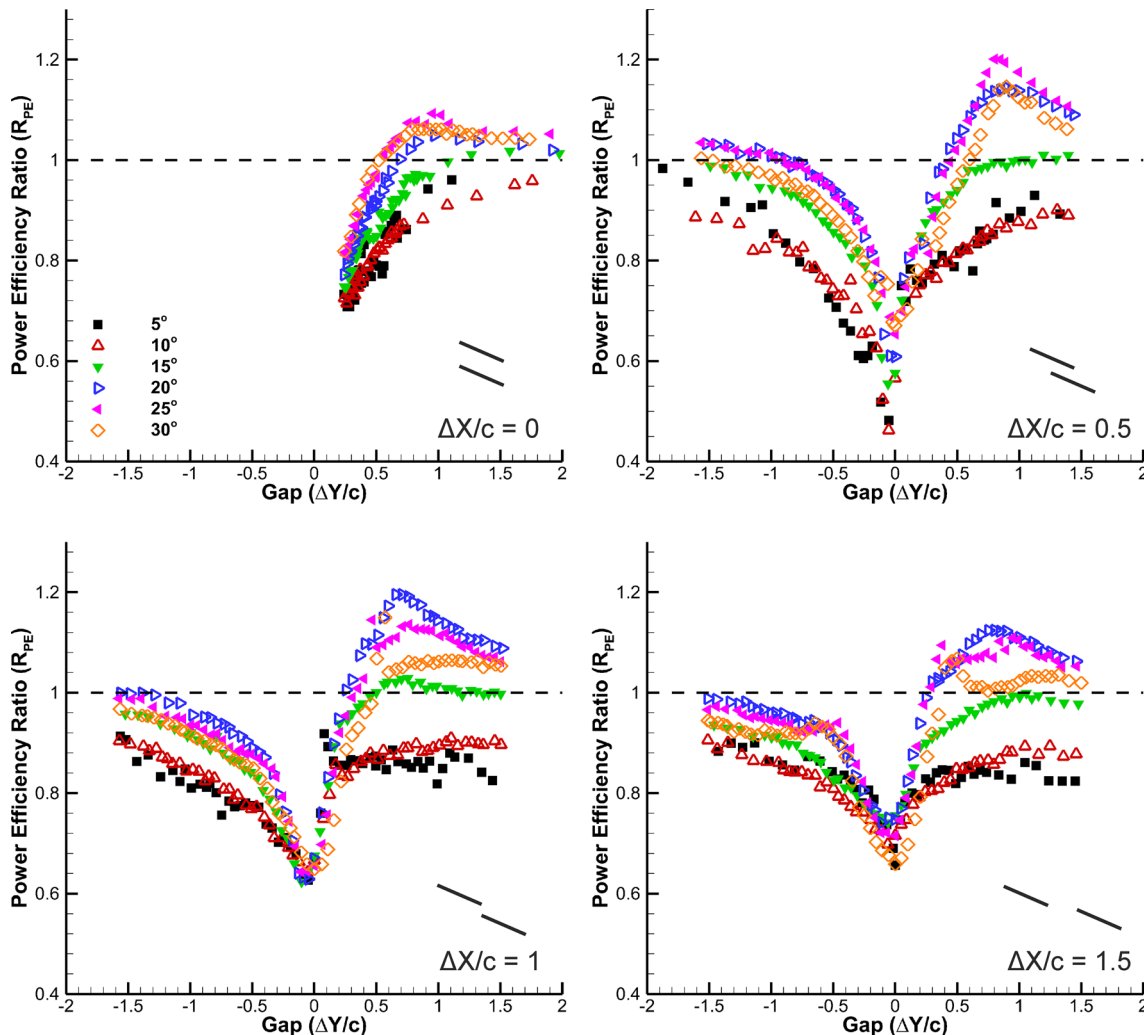


Fig. 8 Ratio of power efficiency of two-wing configurations to that of the single wing. Data points above unity (dashed line) indicate greater power efficiency compared with the single wing

$\Delta Y/c, R_{AE} < 1$ for all angles of incidence (Fig. 7). As $\Delta Y/c$ increases, R_{AE} also increases for all α , and as $\Delta Y/c$ exceeds 0.4, $\alpha = 15^\circ$ to 25° shows a small improvement in aerodynamic efficiency compared with the single wing no greater than approximately 3 %. For $\alpha = 30^\circ$, R_{AE} is observed to straddle a value of 1.0 for $\Delta Y/c > 0.5$. Focusing on the power efficiency ratio data (R_{PE}) for $\Delta X/c = 0$, similar trends are observed as for the lift and drag ratios (Fig. 8). It is noted that $\alpha = 25^\circ$ shows the greatest power efficiency ratio at $\Delta Y/c = 0.95$ over the single wing.

3.2.2 Tandem configurations

We now consider configurations with stagers $\Delta X/c = 0.5$, 1 and 1.5 (see Figs. 5, 6, 7, 8). When $\Delta Y/c > 0$, lift, drag, aerodynamic efficiency and power efficiency ratios follow similar trends to those noted for $\Delta X/c = 0$ but with reduced effect/interaction with increasing $\Delta X/c$. Hence, in the case of $\Delta X/c = 0.5$, the maximum lift ratio ($R_L = 1.32 \pm 0.04$) was observed for $\alpha = 25^\circ$ at $\Delta Y/c = 0.85$ and the lift ratio curves in this region between 25° and 30° are similar. However, $\Delta X/c = 1$, $\alpha = 20^\circ$ is noted to produce the greatest lift ($R_L = 1.27 \pm 0.03$ at $\Delta Y/c = 0.71$), and the drop in lift ratio curves for 25° and 30° suggests a stalled state. When the stagger is increased to $\Delta X/c = 1.5$, the maximum lift ratio is noted to be $R_L = 1.18 \pm 0.03$ at $\alpha = 20^\circ$ and gap $\Delta Y/c = 0.85$. Hence, the maximum lift coefficient achievable for these two-wing configurations decreases with increasing stagger and occurs for varying angle of attack and gaps within a certain limit. Again, the stall angle appears to be delayed significantly (20° to 30°), depending on the $\Delta X/c$ and $\Delta Y/c$. In Fig. 5b, the lift coefficient of the monoplane as well as the total lift coefficient of two configurations that significantly delay the stall is shown. It is seen that the stall angles are 25° and 30° for these cases, although the lift is less than that of the monoplane for pre-stall angles of attack.

For large angles of attack, lift ratio appears to reach a distinct peak before $\Delta Y/c$ reaches 1.0 after which the lift ratio decreases. Drag ratios in this region show almost identical trends to the lift ratio curves with the exception of 5° angle of attack for which lift and drag lie below and above the single-wing threshold, respectively (Figs. 5, 6). When $\Delta Y/c \leq 0$, lift and drag ratios show asymptotic behavior tending toward $R_{L,D} = 1$ as $\Delta Y/c$ decreases for all angles of attack. The minimum lift and drag ratios increase with increasing $\Delta X/c$. In the case of $\alpha = 20^\circ$, for example, the minimum R_L and R_D increase from 0.36 ± 0.01 and 0.35 ± 0.01 , respectively, to 0.55 ± 0.02 and 0.56 ± 0.02 , respectively, in the transition from $\Delta X/c = 0.5$ to 1.5. This effect spreads proportionately above and below this angle of attack, i.e., the effect is more severe for $\alpha = 5^\circ$ and less so for 30° .

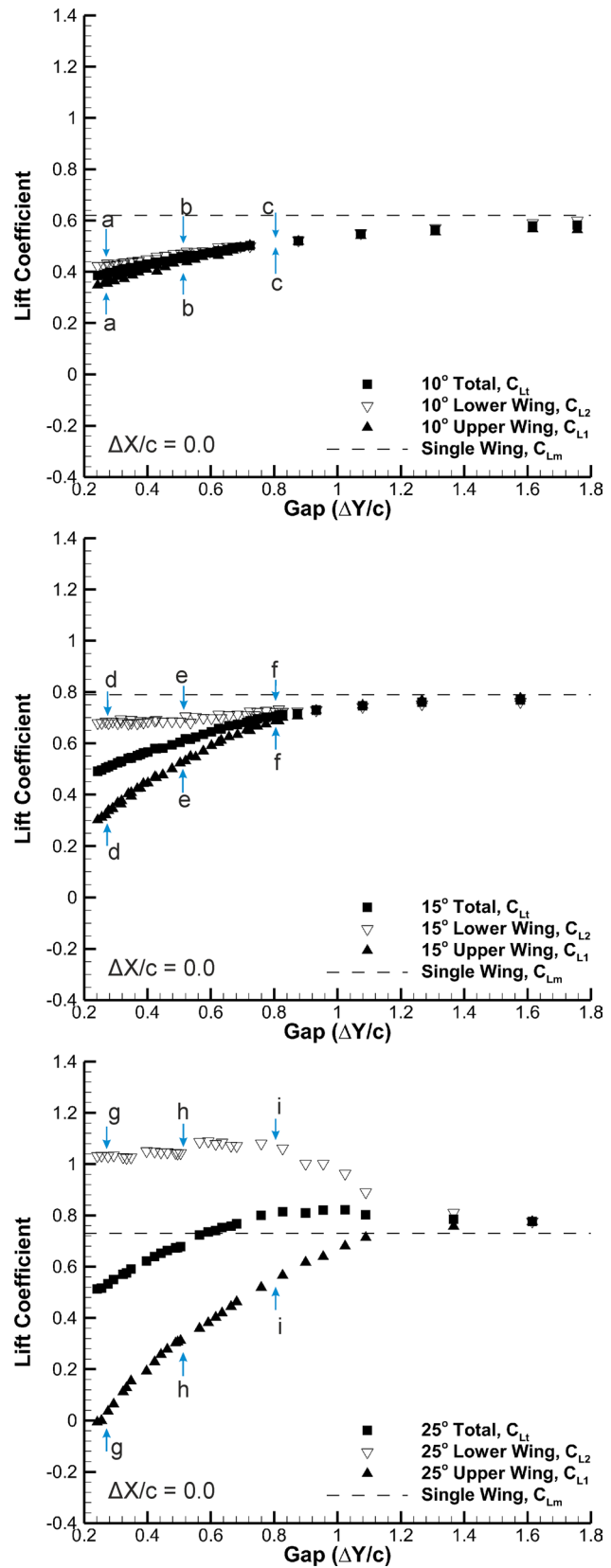


Fig. 9 Lift coefficients for the *upper* and *lower* wing as well as the total lift coefficient. Configurations selected for PIV are highlighted as *a* to *i*; $\Delta X/c = 0$, $\alpha = 25^\circ$

Aerodynamic efficiency ratios for $\Delta X/c = 0.5$ to 1.5 only show marked improvements over the single wing at large angles of attack when $\Delta Y/c > 0$ (Fig. 7). For incidence angles = 5° and 10°, R_{AE} shows generally poor performance. The greatest improvements are noted to occur for $\alpha = 20^\circ$ and 25° which increases with increasing $\Delta X/c$ and reaches a maximum value of $R_{AE} = 1.07 \pm 0.04$ at $\Delta X/c = 1.5$, $\Delta Y/c = 0.3$ and $\alpha = 20^\circ$. Power efficiency ratios for these nonzero staggers exhibit similar trends to those noted for the lift ratios (Figs. 5, 8). It is noted, however, that, in terms of power efficiency ratio, greater

differentiation in flight performance is highlighted between $\alpha = 10^\circ$ and 15° compared with lift coefficient ratio data. Interestingly, the power efficiency ratio data suggest that the greatest improvement in performance over the single wing is achieved when at $\Delta X/c = 0.5$ ($R_{PE} = 1.2 \pm 0.1$ at $\alpha = 25^\circ$ and $\Delta Y/c = 0.8$) and the maximum achievable R_{PE} subsequently decreases with increasing $\Delta X/c$ (contrary to the findings noted for R_{AE}).

The two configurations shown in Fig. 5b have slightly better or the same aerodynamic efficiency at high angles of attack compared with the monoplane, whereas power

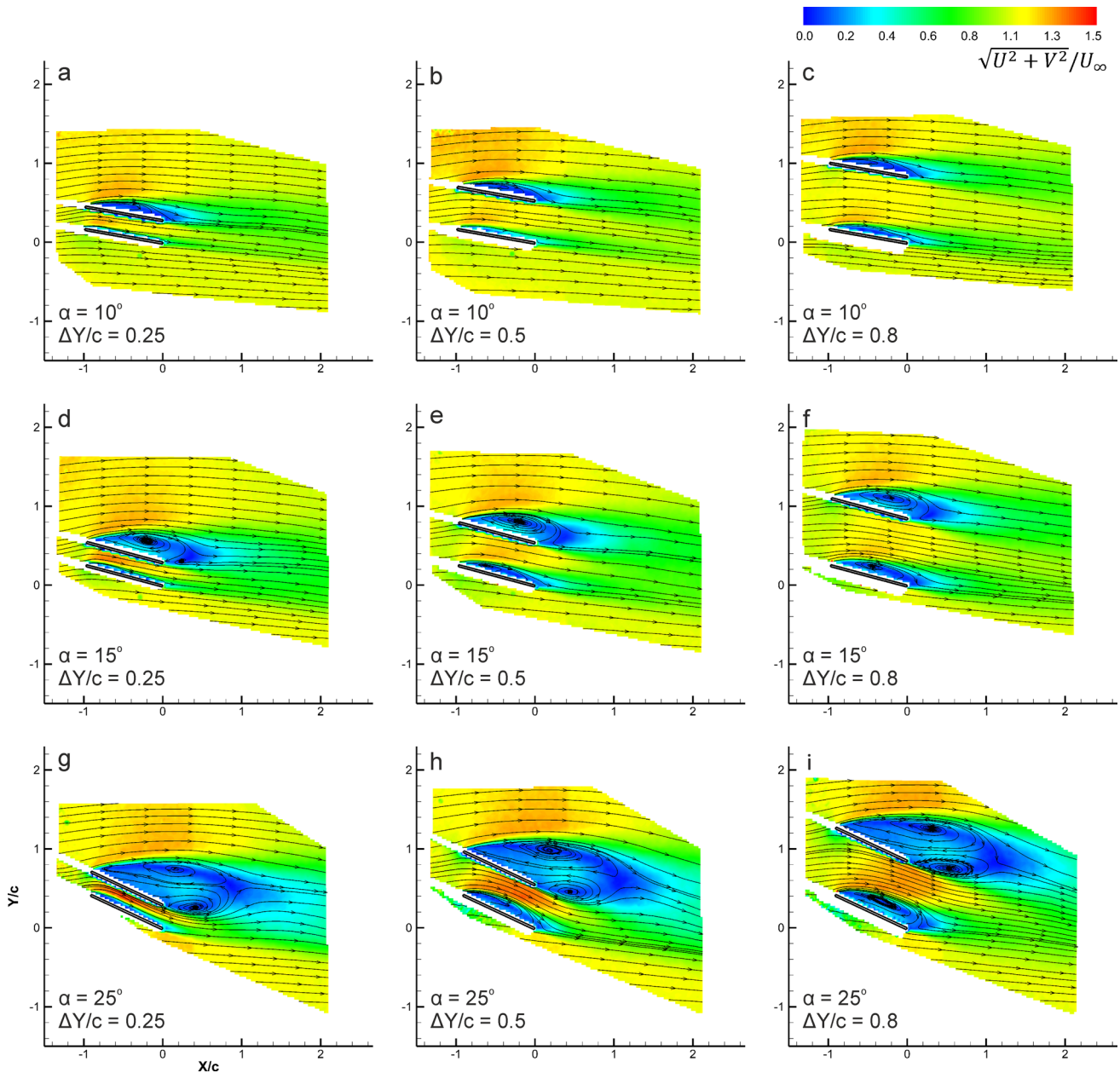


Fig. 10 Non-dimensionalized velocity magnitude for biplane configurations ($\Delta X/c = 0$) selected from Fig. 9 and labelled as *a* to *i*

efficiency exhibits a significant improvement. In general, two-wing configurations show poorer performance compared with the single wing at low angles of attack. However, in certain $\Delta Y/c$ configurations, two-wing performance does show significant improvement over the single wing at large angles of attack ($\alpha \geq 20^\circ$). The stall is significantly delayed, and there is great potential to increase the lift at higher angles of attack while maintaining or improving the aerodynamic and power efficiency. An adaptive configuration having a large gap at small angles of attack and a small gap at moderate/high angles of attack could be considered for future applications.

3.3 Time-averaged two-wing PIV and lift coefficients

We will now consider the flow fields for the biplane and tandem wing configurations and identify five characteristic types of behavior.

3.3.1 Biplane configuration

Figure 9 shows the lift coefficient for the individual wings as a function of $\Delta Y/c$ for $\alpha = 10^\circ, 15^\circ$ and 25° . Figures 10 and 11 present accompanying PIV velocity magnitude and vorticity fields, respectively, for selected values of gap:

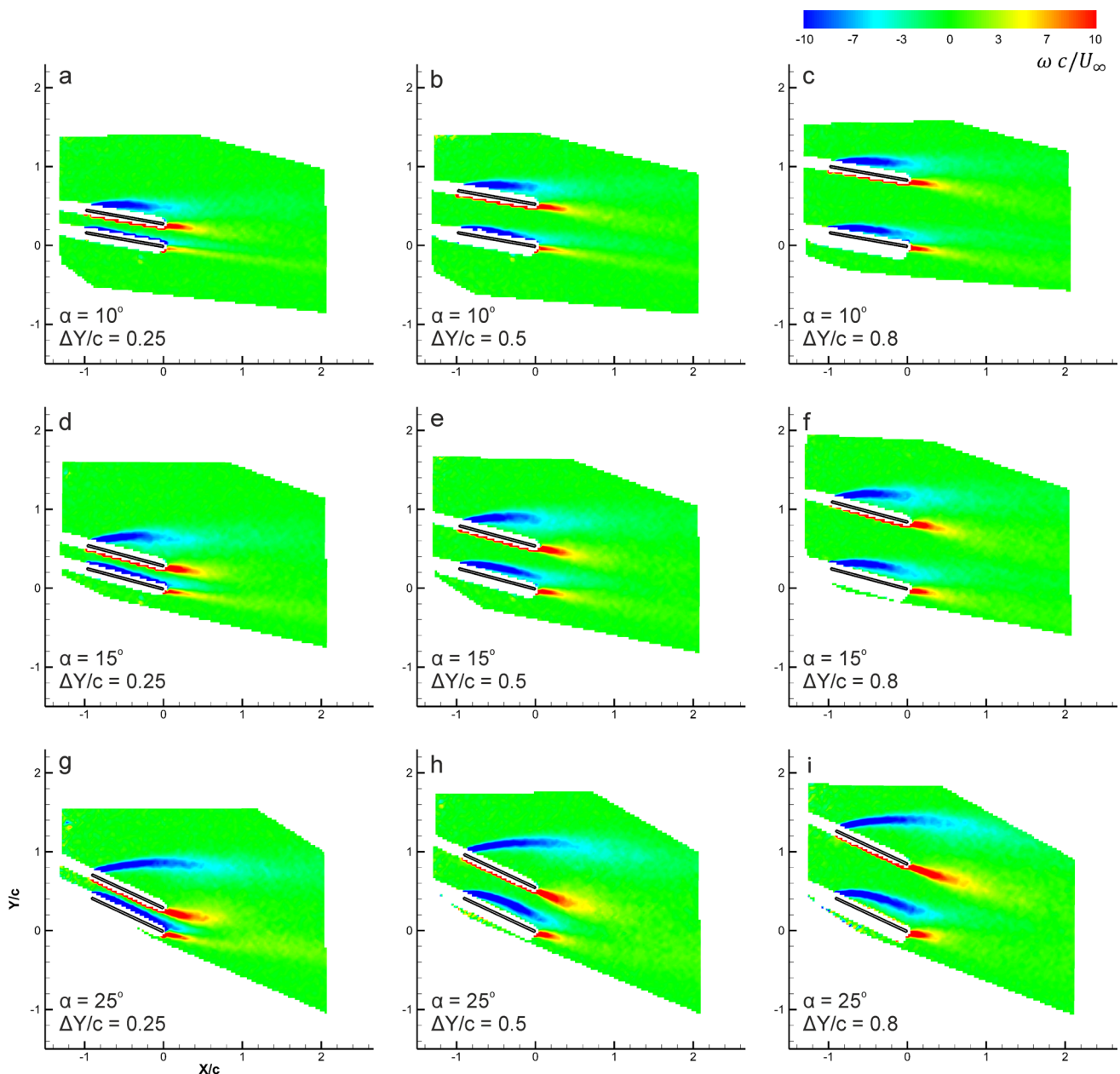


Fig. 11 Non-dimensionalized vorticity for biplane configurations ($\Delta X/c = 0$) selected from Fig. 9 and labelled as *a* to *i*

$\Delta Y/c = 0.25, 0.5$ and 0.8 . These PIV cases are highlighted as ‘a’ to ‘i’ in Fig. 9, and the dashed line corresponds to the single-wing value. In each case, the lower wing produces greater lift than the upper wing. This difference increases with angle of incidence. The velocity magnitude fields indicate that in each case, particularly the configuration labelled

‘g’ ($\alpha = 25^\circ$ and $\Delta Y/c = 0.25$), the upper wing forces the flow over the lower wing closer to the surface which in turn encourages partial reattachment of the separated shear layer from the leading edge of the lower wing. This effect is made clear in the vorticity fields. In the region between the wings, particularly for small crosswise separations and large α , there

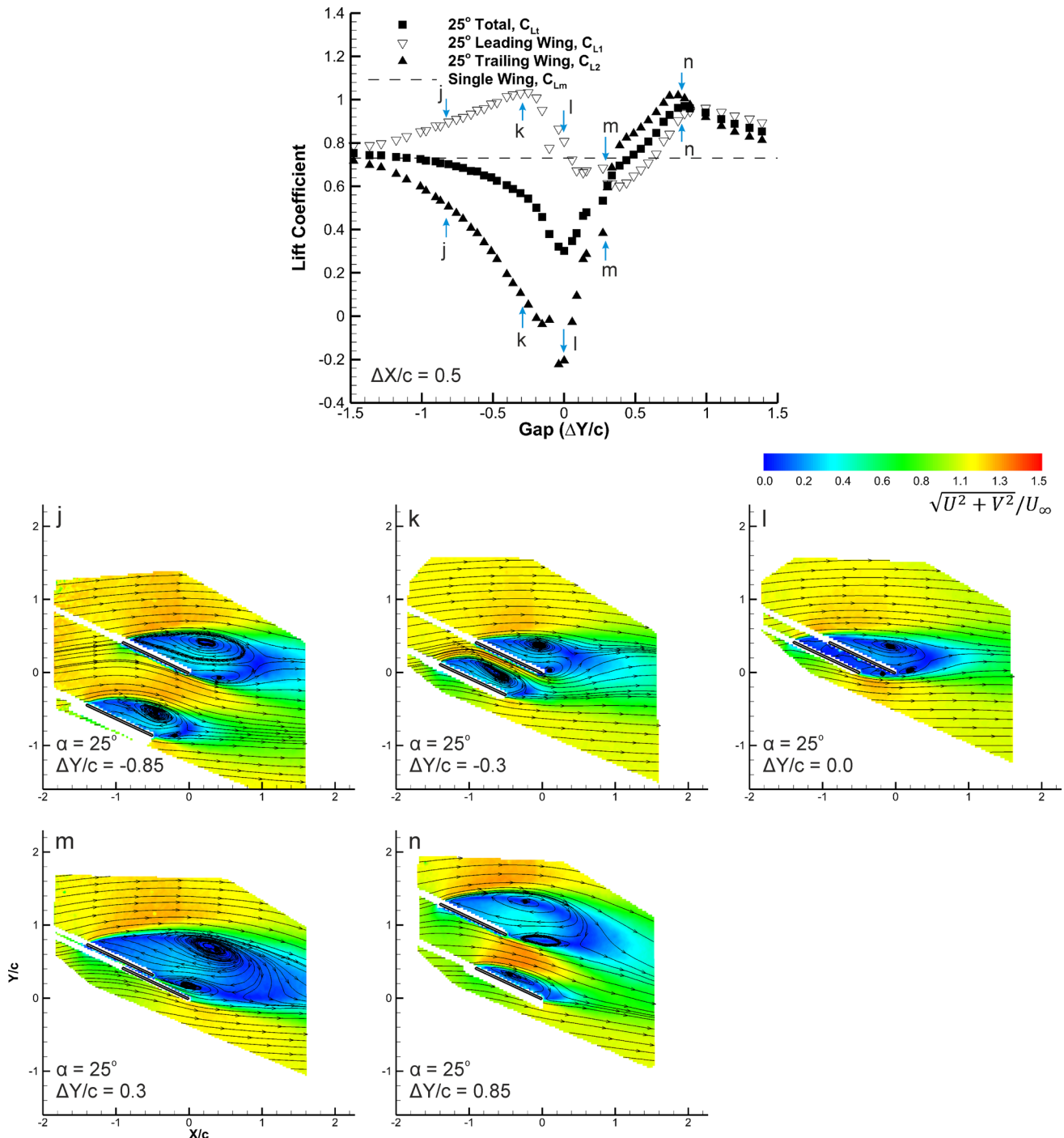


Fig. 12 Lift coefficients for separate wings in tandem ($\Delta X/c = 0.5$) at 25° angle of attack (top). Configurations selected for PIV are indicated as *j* to *n*. Normalized velocity magnitude for *j* to *n* are presented (bottom)

is strong high-speed flow. As per the Bernoulli equation, high-speed flow is associated with low pressure resulting in suction which would explain the gain in lower wing lift and the loss in upper wing lift. This type of flow field where high-speed flow interacts with both wing surfaces is termed “high-speed inter-wing flow of type 1” (IF1). Comparing the $\alpha = 25^\circ$ configurations in Fig. 10 with the velocity magnitude fields of the single wing in Fig. 4, the wakes of the upper wing are comparable in size to that of the single wing.

3.3.2 $\Delta X/c = 0.5$

Figures 12 and 13 present selected velocity magnitude and vorticity fields for $\Delta X/c = 0.5$ at $\alpha = 25^\circ$ for a range of $\Delta Y/c$ values labelled ‘j’ to ‘n’ with the leading, trailing and total wing lift coefficient data presented in Fig. 12 (top). Again, the single-wing lift coefficient value is represented by a dashed line. The configuration labelled ‘n’ ($\Delta Y/c = 0.85$) produces a maximum value of total lift coefficient of $C_{Lt} = 0.71 \pm 0.01$. Conversely the configuration labelled ‘j’ ($\Delta Y/c = -0.85$) does not exhibit any improvement in lift over the single wing. It is important to note that between these configurations, the leading and trailing wings switch between being ‘upper’ and ‘lower’ wings.

Similar effects to those noted for configurations labelled ‘g’ to ‘i’ in Figs. 9, 10, 11 are shown to occur in ‘n’ of Figs. 12 and 13. The leading wing has a significantly larger wake which tends downward and toward the trailing wing, and the high velocity flow between the wings encourages a less separated flow over the lower wing. Comparing the position of this high-speed flow in relation to the leading (upper) wing in ‘n’ with the position observed in ‘j’ relative to the trailing (upper) wing, we see that in ‘n’ the position is aft of the upper wing’s trailing edge and in ‘j’ the position is coupled with the lower surface of the upper wing. This demonstrates that the loss in lift experienced by the upper wing is strongly dependent on its proximity to the high-speed flow. The type of flow observed in ‘n’ is termed ‘high-speed inter-wing flow of type 2’ (IF2). In the transition from ‘j’ to ‘k’ (increasing $\Delta Y/c = -0.85$ to -0.3), the IF1 effect is even stronger and is fundamentally different because the position of the trailing wing is now in the high-speed flow and therefore subject to very low C_L . Analysis of configurations ‘j’ and ‘k’ in Figs. 12 and 13 also reveals that the wake of the trailing wing is reduced in ‘k’ and the leading-edge shear layer of the leading wing traverses along the lower surface of the trailing wing. The leading wing experiences a local maximum in lift coefficient at ‘k’ after

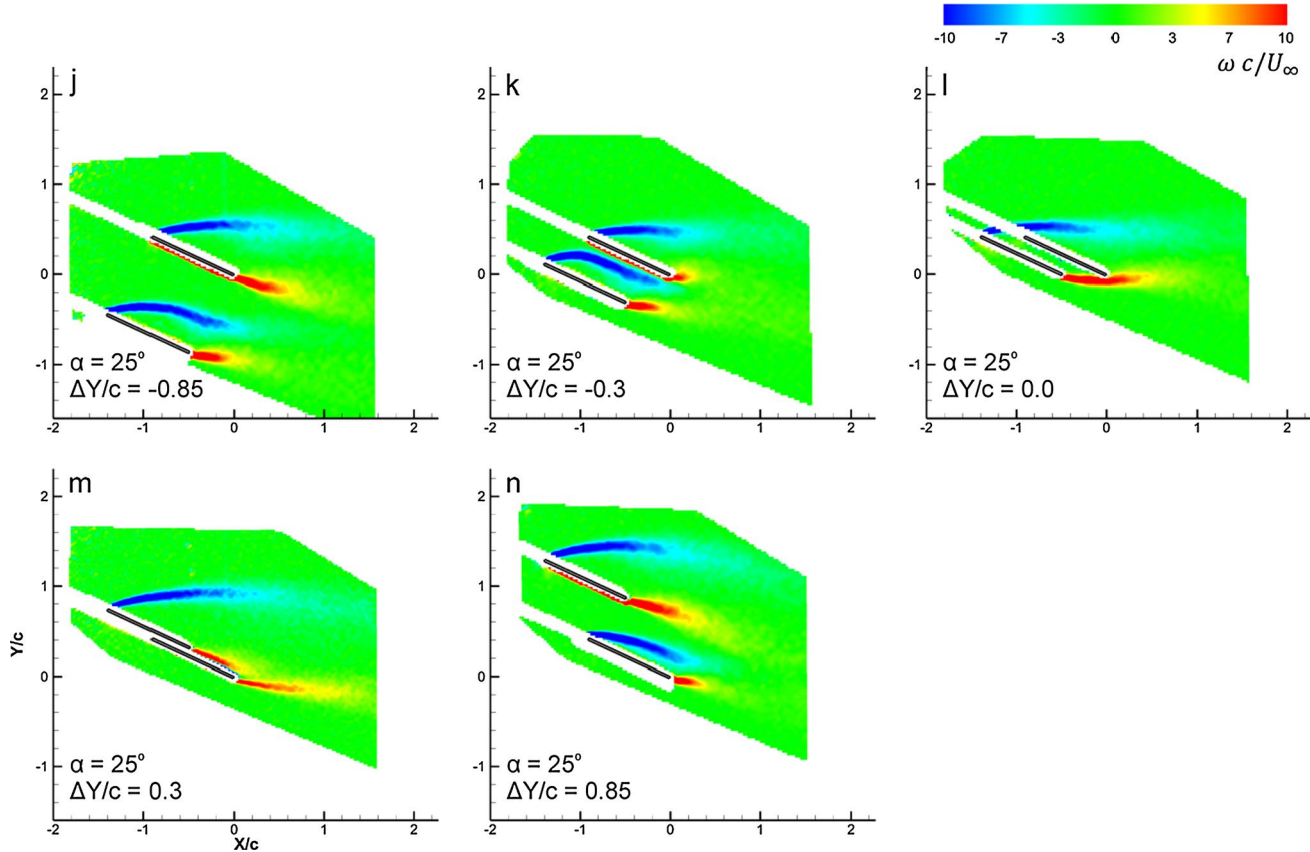


Fig. 13 Non-dimensionalized vorticity for selected PIV configurations *j* to *n* for tandem wings ($\Delta X/c = 0.5$) at 25° angle of attack

which increasing $\Delta Y/c$ demonstrates a loss in lift coefficient which is likely due to the coincidence of the leading-edge shear layer of the leading wing with the trailing wing's leading edge resulting in merging of the two wakes.

Configurations labelled 'l' and 'm' ($\Delta Y/c = 0$ and 0.3) are of interest due to the similarity of the merged wakes to

single-wing behavior. When the wings are in direct tandem, the trailing wing is observed to lie inside the wake of the leading wing; the leading wing produces lift comparable to the single wing, and the trailing wing produces slightly negative lift. The resultant total lift coefficient is roughly half that of the single wing. This type of tandem wing flow

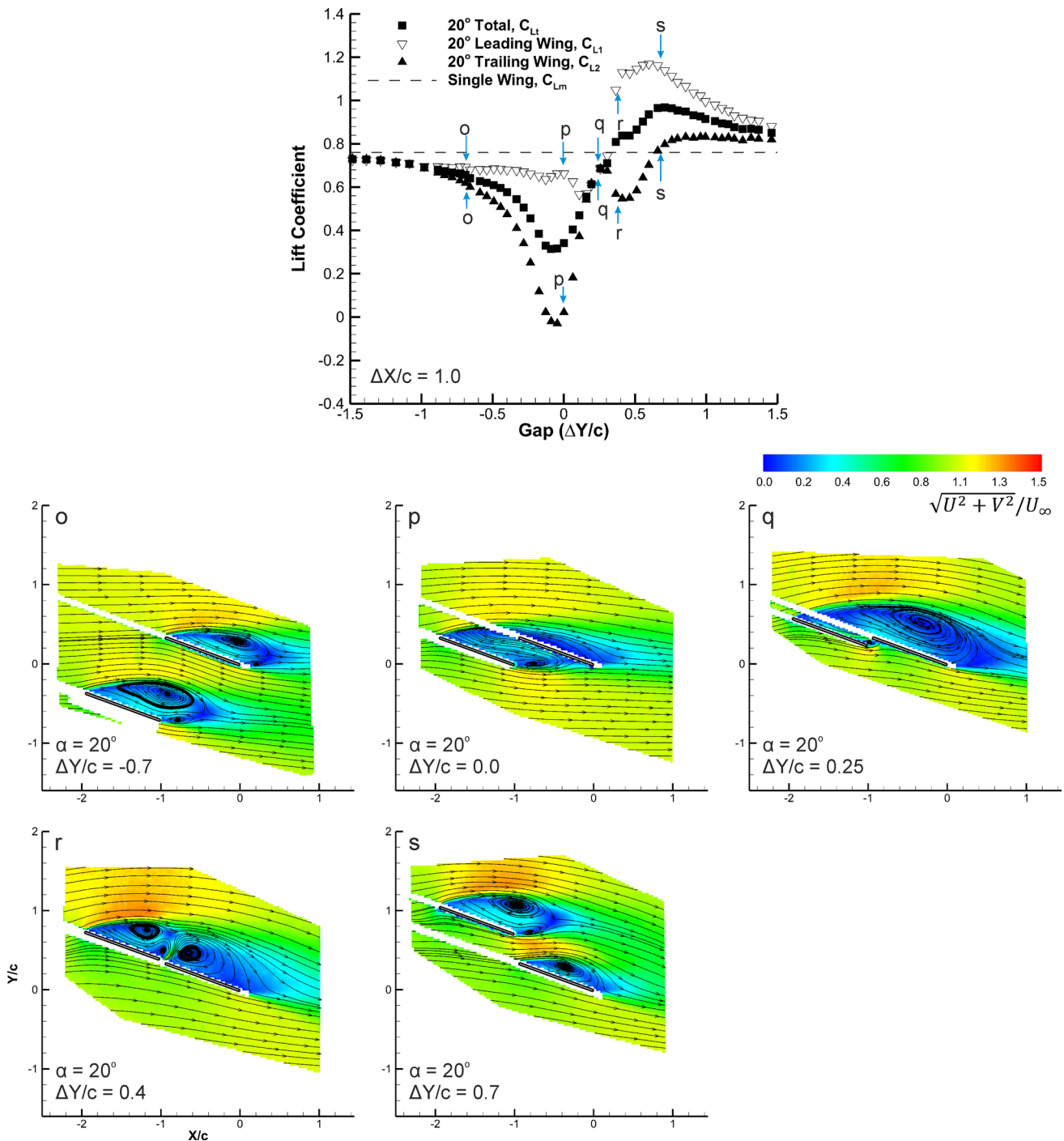


Fig. 14 Lift coefficients for separate wings in tandem ($\Delta X/c = 1$) at 20° angle of attack (top). Configurations selected for PIV are indicated as *o* to *s*. Normalized velocity magnitude for *o* to *s* is presented (bottom)

in which the wakes of the wings are merged due to the aft wing residing in the wake of the fore wing is termed as a ‘merged wake of type 1’ (MW1). When $\Delta Y/c = 0.3$ (point ‘m’), the wings act as one large wing and the lift coefficients of both wings are comparable to one another and close to the single-wing value with a slight reduction due to the overlap. It is noted that for ‘m’, the trailing edge of the leading wing possesses a shear layer which is closely coupled to the trailing wings’ upper surface signifying interwing flow (see Fig. 13). This flow type, with unionized wakes and both wings’ lower surfaces being subject to the freestream, is termed as a ‘merged wake of type 2’ (MW2).

3.3.3 $\Delta X/c = 1$ and 1.5

Figures 14, 15 and 16 present selected velocity magnitude, vorticity field and velocity SD squared (labelled ‘o’ to ‘s’) with lift coefficient data for $\Delta X/c = 1$ at $\alpha = 20^\circ$. Figures 17 and 18 present data with the same $\Delta Y/c$ and α values as Figs. 14, 15 and 16 but with $\Delta X/c = 1.5$ (configurations are labelled ‘t’ to ‘x’). These figures shall be discussed together as there are similarities in the force coefficient versus $\Delta Y/c$ data. However, we first wish to draw attention to the drastic change in force coefficient behavior

in the transition from $\Delta X/c = 0.5$ to 1.0 (presented at the top of Figs. 12 and 14). It is important to note that these two cases have differing angle of attack but were chosen due to their proximity to the stall angle as discussed in Sect. 3.2. When $\Delta X/c = 0.5$ (Fig. 12), for $\alpha \geq 20^\circ$ the leading wing (C_{L1}) produces more lift than the single wing for $\Delta Y/c < 0$ and less lift than the trailing wing when $\Delta Y/c > 0.4$. With $\Delta X/c = 1$ (Fig. 14), this behavior is no longer observed. Instead, the leading wing always produces greater lift than the trailing wing and is only greater than the single-wing value when discussed in Sect. 3.2 $\Delta Y/c > 0.3$. The trailing wing has the greater lift than the leading wing in a finite interval of $\Delta Y/c$ for $\Delta X/c = 0.5$ (Fig. 12); however, this was not observed for $\Delta X/c = 1$ and 1.5 for any angle of attack. Comparison of the flow fields labelled ‘j’ to ‘n’ in Figs. 12 and 13 with the equivalent data labelled ‘o’ to ‘s’ in Figs. 14 and 15 coupled with these observations leads us to characterize the $\Delta X/c = 0.5$ configurations as a quasi-biplane state so that the tandem state is only true for $\Delta X/c \geq 1$.

We now focus on tandem configurations $\Delta X/c = 1$ and 1.5 (Figs. 14, 15, 16, 17, 18). Comparing configuration ‘o’ in Figs. 14 and 15 with ‘t’ in Figs. 17 and 18 ($\Delta Y/c = -0.7$), the velocity magnitude and vorticity fields are observed to be similar and fall into the category IF1.

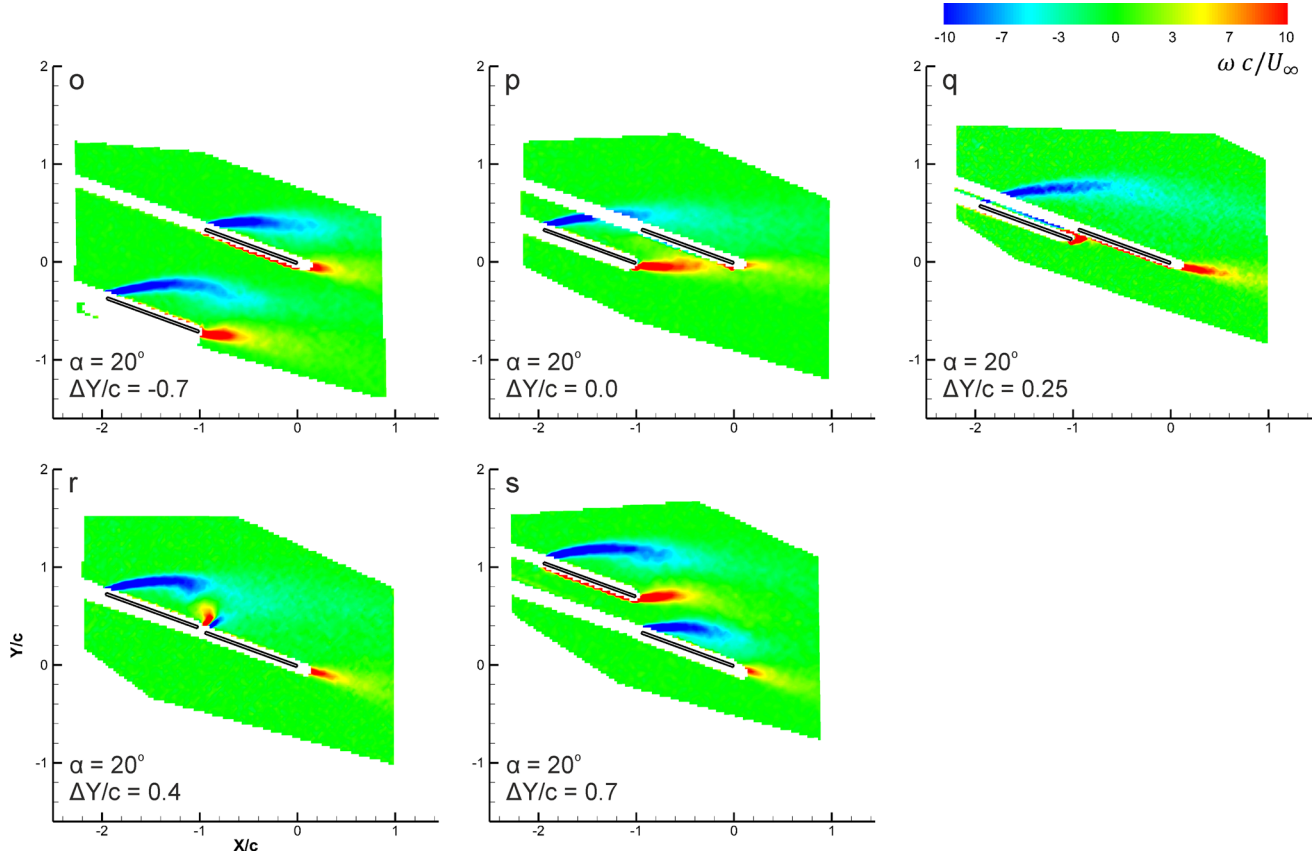


Fig. 15 Non-dimensionalized vorticity for selected PIV configurations *o* to *s* for tandem wings ($\Delta X/c = 1$) at 20° angle of attack

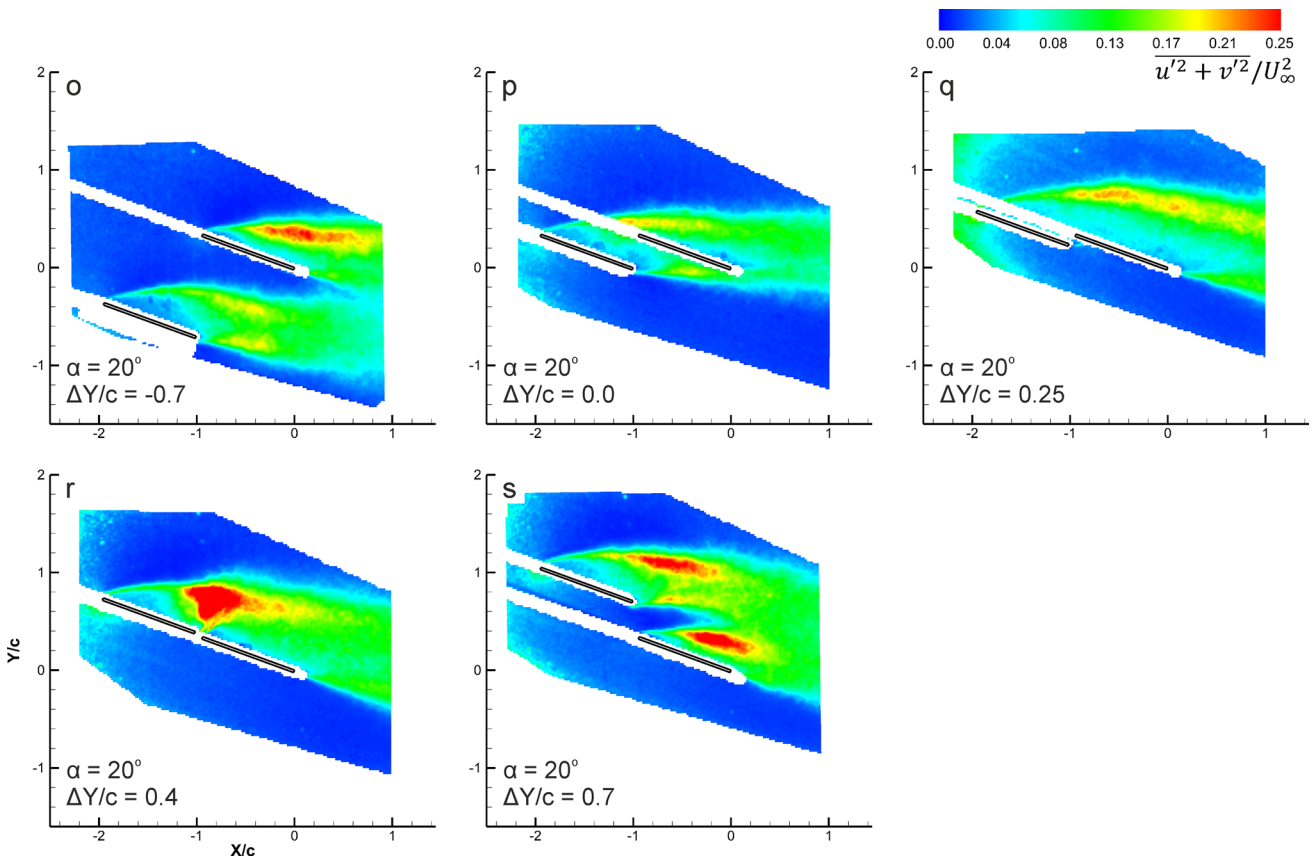


Fig. 16 Standard deviation of velocity squared for selected PIV configurations *o* to *s* for tandem wings ($\Delta X/c = 1$) at 20° angle of attack

However, the leading wing produces greater lift than the trailing wing at ‘*o*’, whereas the converse is true for ‘*t*’. The wake of the leading wing is of similar size and shape; however, the wake of the trailing wing is somewhat reduced in the case of ‘*t*’ ($\Delta X/c = 1.5$), and the inter-wing flow is slower which may explain the difference in lift coefficient polarity. The vorticity data for these configurations (‘*o*’ to ‘*t*’) confirm this observation in terms of the leading-edge shear layer of the trailing wing. The leading-edge shear layer of the leading wing is drawn toward the lower surface of the trailing wing which is likely due to the accelerated inter-wing flow resulting in a low pressure region in the vicinity of the trailing wing’s lower surface.

When the wings are in direct tandem ($\Delta Y/c = 0$; cases labelled ‘*p*’ and ‘*u*’ in Figs. 14, 15, 16, 17, 18), the wakes merge and fall into the category MW1. Similar trends in lift coefficient behavior are observed with lift coefficient values differing more in the case of $\Delta X/c = 1$. In the transition from $\Delta X/c = 1$ to 1.5 for $\Delta Y/c = 0$, the leading wing lift coefficient decreases from $C_{L1} = 0.66 \pm 0.01$ to $C_{L1} = 0.62 \pm 0.01$ and the trailing wing lift coefficient increases from $C_{L2} = 0.022 \pm 0.002$ to $C_{L2} = 0.23 \pm 0.01$. Analysis of the velocity magnitude and vorticity fields indicates stronger reverse flow between the wings in ‘*p*’

compared with ‘*u*’ which may explain the difference in leading wing lift coefficients. Examining the flow fields in relation to the trailing wing reveals that in the case of ‘*u*’ ($\Delta X/c = 1.5$), the trailing-edge shear layer of the leading wing impinges upon the trailing wing’s lower surface further from its trailing edge compared with ‘*p*’. This implies that a larger portion of the trailing wing’s lower surface in ‘*u*’ is subject to the freestream flow than ‘*p*’ thus resulting in greater lift. It is also apparent in the velocity magnitude fields that the proximity of the wake in ‘*u*’ to the upper surface of the trailing wing is less than that in ‘*p*’ implying lower pressure and therefore greater lift.

Comparing configurations ‘*q*’, ‘*r*’ and ‘*s*’ in Figs. 14 and 15 with the equivalent configurations in Figs. 17 and 18 (‘*v*’, ‘*w*’ and ‘*x*’) reveals the most fundamental differences in aerodynamic behavior discussed so far. Looking specifically at the velocity magnitude and vorticity fields for $\Delta Y/c = 0.25$ (‘*q*’ and ‘*v*’), it is clear that as $\Delta X/c$ increases from 1.0 to 1.5, the leading and trailing wings’ transition from behaving as a single wing [with a minor shear layer between the trailing edge of the leading wing and the leading edge of the trailing wing and a unified wake (categorized as MW2)] to two partially divided wakes and the trailing wing develops a leading-edge shear

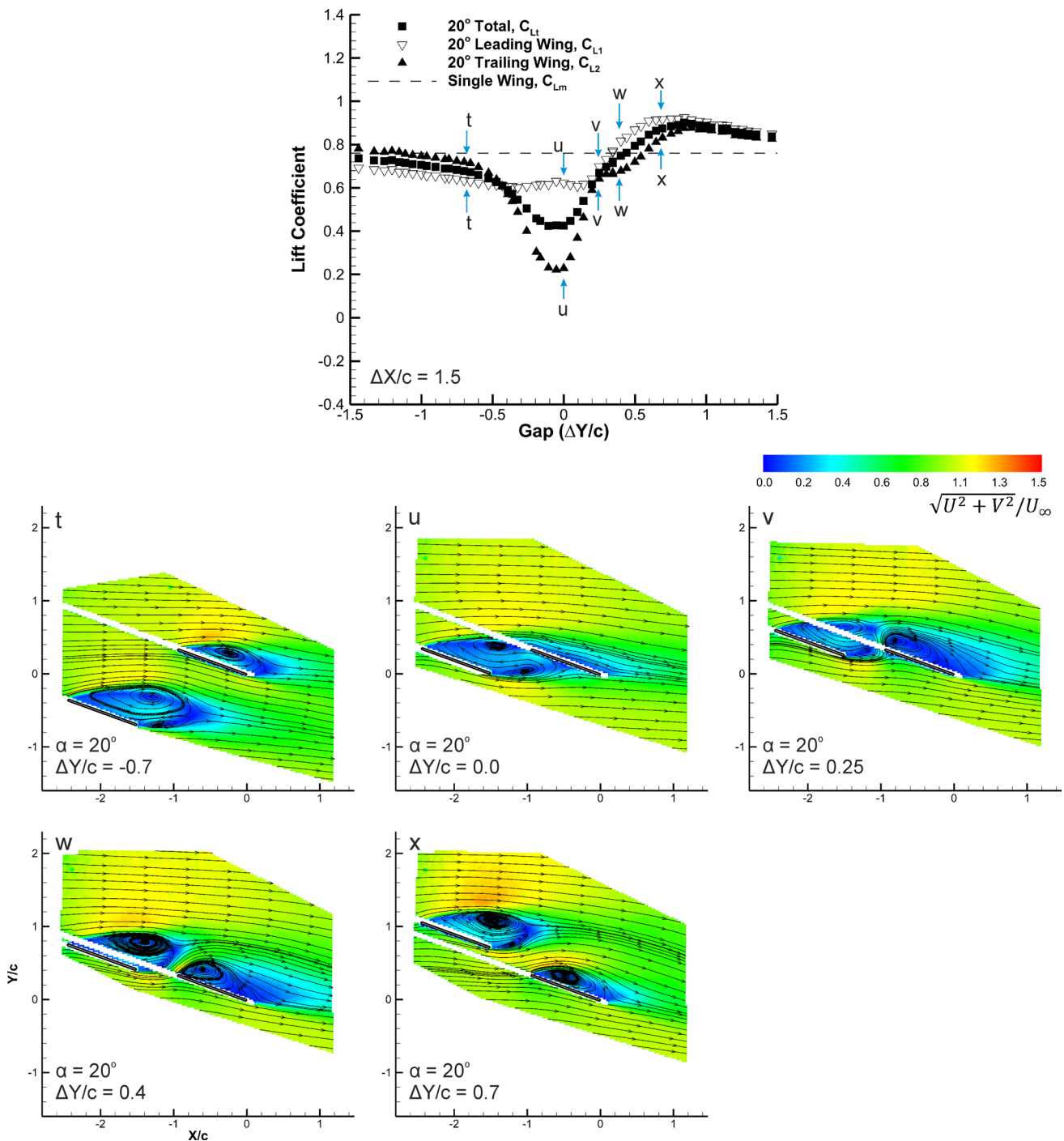


Fig. 17 Lift coefficients for separate wings in tandem ($\Delta X/c = 1.5$) at 20° angle of attack (top). Configurations selected for PIV are indicated as t to x . Normalized velocity magnitude for t to x is presented (bottom)

layer and there is a certain amount of inter-wing flow. This new type of flow behavior is termed ‘quasi-merged wakes with partial inter-wing flow of type 3’ (IF3). In both cases, the shear layer emanating from the trailing edge of the leading wing impinges directly onto the trailing wing’s leading edge. Values of lift coefficient between

leading and trailing wing are somewhat similar for these two cases (‘q’ and ‘v’).

When $\Delta X/c = 1$ and $\Delta Y/c = 0.4$ (labelled ‘r’ in Figs. 14 and 15), a local minimum in trailing wing lift coefficient is noted. This effect is weaker for the case $\Delta Y/c = 0.4$ when $\Delta X/c = 1.5$ (labelled ‘w’ in Figs. 17 and 18). Velocity

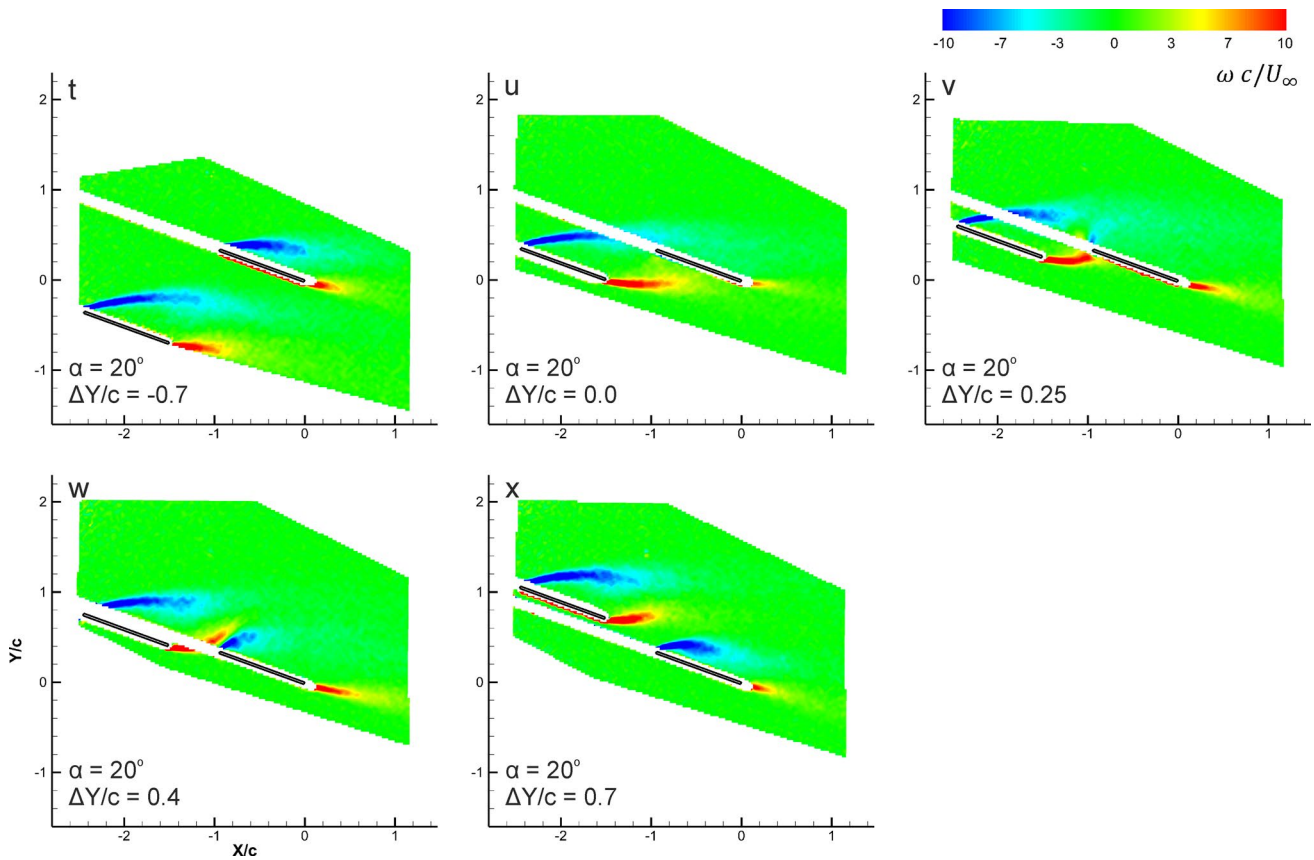


Fig. 18 Non-dimensionalized vorticity for selected PIV configurations t to x for tandem wings ($\Delta X/c = 1.5$) at 20° angle of attack

magnitude and vorticity fields indicate an inter-wing jet encroaching the wake in the case labelled ‘r’, categorized as IF3, with discrete shear layers emanating from the trailing edge of the leading wing and the leading edge of the trailing wing. An interesting observation can be made from the velocity magnitude SD squared data for the case labelled ‘r’ in Fig. 16 which shows that the IF3 flow behavior exhibits a region of high flow unsteadiness. Similar unsteady interactions will be discussed later in the paper. The transition to $\Delta X/c = 1.5$ (‘w’) reveals stronger inter-wing flow dividing the wing wakes, and the lift coefficients of the leading and trailing wing reduce and increase, respectively. It was previously noted that the largest R_{AE} observed occurred at $\Delta X/c = 1.5$, $\Delta Y/c = 0.3$ and $\alpha = 20^\circ$ which places this phenomena between configurations ‘v’ and ‘w’ in terms of the $\Delta Y/c$. Hence, improved aerodynamic efficiency can be associated with the flow type IF3.

When $\Delta Y/c$ reaches 0.7, configurations ‘s’ and ‘x’ ($\Delta X/c = 1$ and 1.5, respectively) both exhibit the flow type categorized as IF2; hence, the leading (upper) wing is less affected by the high-speed inter-wing flow and therefore does not suffer a loss in lift. Contrary to the observations made for $\Delta X/c = 0.5$ in which, for large $\Delta Y/c$ (-0.85 and

0.85 labelled ‘j’ and ‘n’ in Figs. 12 and 13), the trailing wing exhibits a reduced wake and the leading wing exhibits an enlarged wake for $\Delta Y/c = 0.85$ and vice versa when $\Delta Y/c = -0.85$. For $\Delta X/c = 1$ and 1.5 with $\Delta Y/c = -0.7$ and 0.7 (cases labelled ‘o’, ‘s’, ‘t’ and ‘x’ in Figs. 14, 15, 16, 17, 18), the trailing wing always exhibits the strongly reduced wake regardless of whether $\Delta Y/c = 0.7$ or $\Delta Y/c = -0.7$. This may explain the shift in dominance of lift production between leading and trailing wing noted previously for the transition in lift coefficient behavior as $\Delta X/c$ increases from 0.5 to ≥ 1 .

3.3.4 Lift peak ($\Delta X/c = 1.5$)

It is noted in Fig. 17 that the trailing wing has a local maximum in lift as the gap becomes positive (case ‘w’) for $\Delta X/c = 1.5$ and $\alpha = 20^\circ$. Similar peaks in lift exist for other angles of attack as shown in Fig. 19 for $\alpha = 25^\circ$ and 30° . It is interesting that these peaks occur at the same gap, $\Delta Y/c = 0.4$. Figure 20 shows time-averaged velocity magnitude, vorticity and velocity SD squared data for $\Delta X/c = 1.5$, $\Delta Y/c = 0.4$ and $\alpha = 20^\circ$, 25° and 30° . The corresponding lift coefficient versus $\Delta Y/c$ can be found

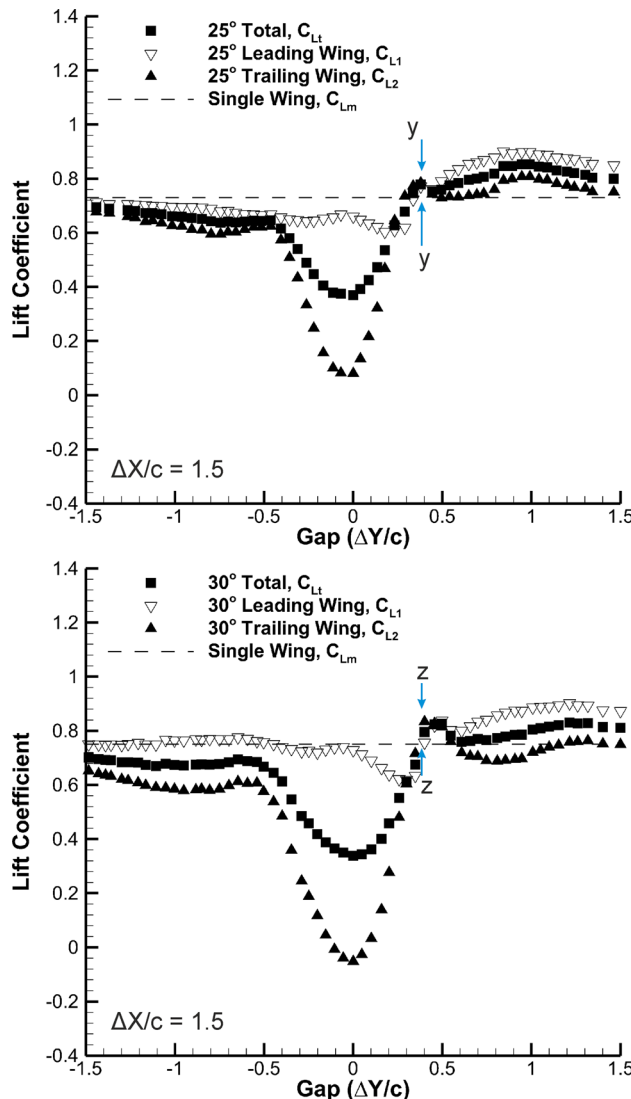


Fig. 19 Lift coefficient for tandem wings ($\Delta X/c = 1.5$) at $\alpha = 25^\circ$ and 30° . Configurations selected for PIV are denoted as *y* and *z* for comparison of flow fields at $\Delta Y/c = 0.4$

in Figs. 17 and 19 labelled ‘w’, ‘y’ and ‘z’. The total lift coefficient is noted to increase from $C_{L1} = 0.75 \pm 0.01$ to 0.78 ± 0.01 to 0.80 ± 0.01 as α increases from 20° to 25° to 30° , respectively. The velocity magnitude data shown for configurations labelled ‘w’ (previously categorized as IF3), ‘y’ and ‘z’ reveal the inter-wing flow being forced to greater acute angles from the freestream direction as α increases and the wake of the trailing wing becomes larger. The vorticity data show that as α increases, the trailing-edge shear layer of the leading wing tends to impinge directly onto the trailing wing’s leading edge. An interesting observation can, once again, be made from the velocity magnitude SD squared data which show that as α increases, the region of high unsteadiness unifies from separate regions in the configuration labelled ‘w’ to one region in the configurations

labelled ‘y’ and ‘z’, i.e., the IF3 flow type has an intrinsic tendency to produce a merged region of high unsteadiness as the inter-wing flow is forced to greater acute angles.

3.4 Unsteady force and instantaneous flow

Figure 21 presents instantaneous velocity magnitude fields for $\Delta X/c = 0.5$ and $\Delta Y/c = -0.06$ (close to being directly in tandem) at 30° angle of attack. This configuration was selected because it exhibits a surge in unsteady forces. Also shown are comparable single-wing instantaneous velocity magnitude data (right column). Lift coefficient data are presented at the top of the figure with lift coefficient SD represented by bars. Figure 22 presents instantaneous velocity magnitude fields for $\Delta X/c = 1.5$ and $\Delta Y/c = 0.4$ at 30° angle of attack which also exhibits a maximum in the SD of the lift coefficient.

Time-dependent lift coefficient forces were oscillatory in nature. By applying an impulsive force to the wing tip and measuring the power spectral density as a function of frequency from the decaying signal ex situ, the resonant frequency of the wing-force balance structure was found to be between 24 and 25 Hz. At 30° , the single-wing time-averaged lift coefficient is $C_{Lm} = 0.76 \pm 0.02$ with a SD of $\sigma_{CLm} = 0.05$. For the tandem configuration with $\Delta X/c = 0.5$, $\Delta Y/c = -0.06$ and $\alpha = 30^\circ$ (Fig. 21 highlighted in red), the leading wing exhibits $C_{L1} = 0.93 \pm 0.02$ and $\sigma_{CL1} = 0.25$ and the trailing wing, $C_{L2} = -0.07 \pm 0.01$ and $\sigma_{CL2} = 0.60$. It is clear from these observations that there is a marked difference in unsteady forces for the tandem configuration when $\Delta Y/c = -0.06$ compared with other values of $\Delta Y/c$ with fixed $\Delta X/c = 0.5$ and $\sigma = 30^\circ$ as well as the single wing at 30° angle of attack. Examination of the instantaneous flow fields in Fig. 21 reveals that the single wing’s wake and separated shear layer geometry maintain relatively consistent size and shape through time. For the tandem configuration, drastic changes in wake and shear layer shape are observed. The shear layer passing over the leading edge of the trailing wing is observed to reattach and detach to the upper surface of the trailing wing. This unsteady flow is therefore characterized by switching between stalled and unstalled states of the trailing wing and hence the large SD of the trailing wing lift coefficient. In light of the previous discussion, this configuration falls under the MW1 category.

Examination of the second unsteady case for $\Delta X/c = 1.5$ (Fig. 22) reveals that, in general, the SD of the lift coefficient for the trailing wing has increased relative to $\Delta X/c = 0.5$ for all $\Delta Y/c$ values. The maximum value of SD is at $\Delta Y/c = 0.4$ (highlighted in red in Fig. 22) at which the leading wing exhibits $C_{L1} = 0.76 \pm 0.02$ and $\sigma_{CL1} = 0.29$ and the trailing wing, $C_{L2} = 0.83 \pm 0.02$ and $\sigma_{CL2} = 0.43$. Incidentally, at $\Delta Y/c = 0.4$, a localized maximum in

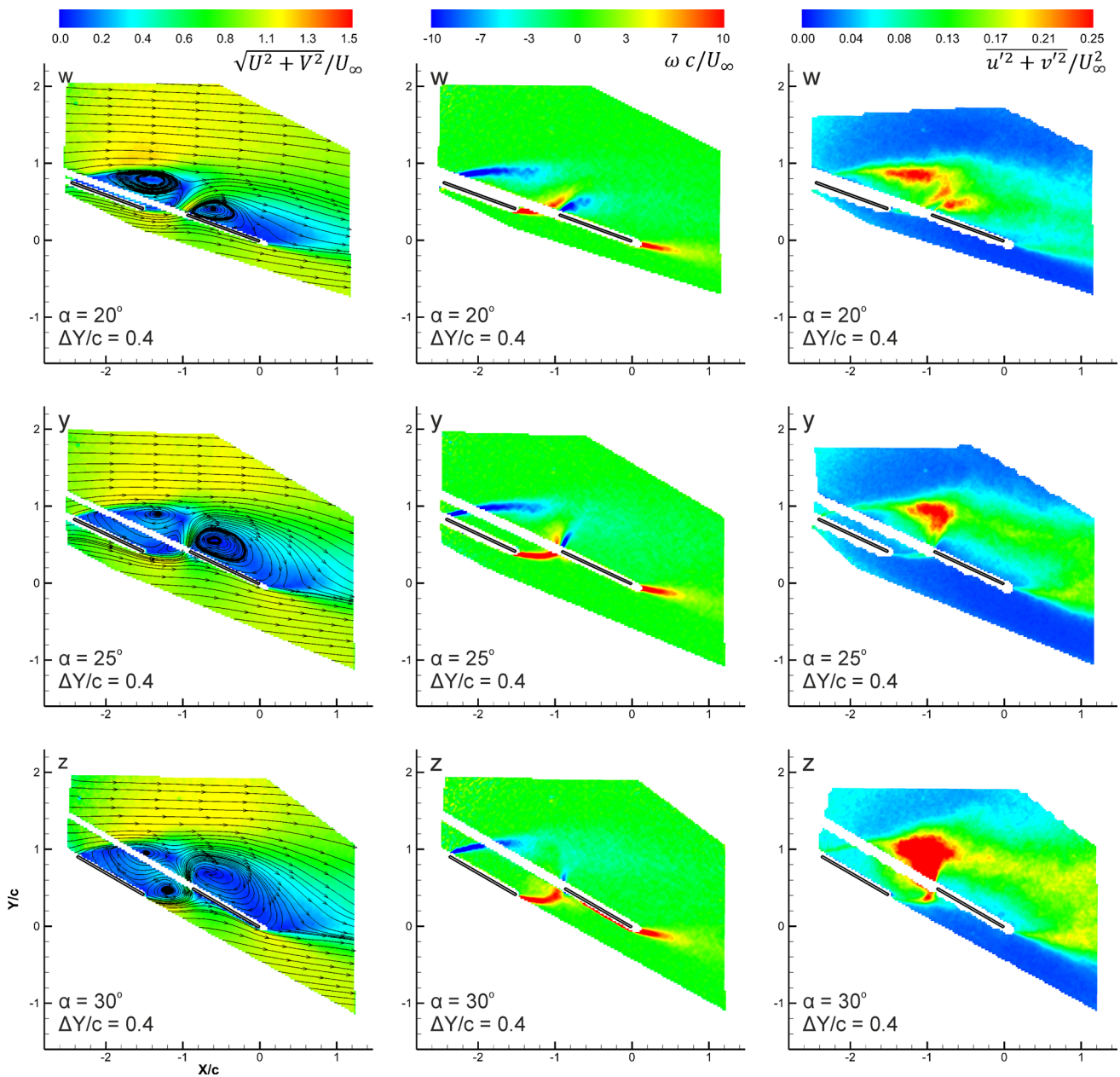


Fig. 20 Velocity magnitude and streamlines (*left*), vorticity (*center*) and standard deviation of velocity squared (*right*) for tandem configurations *w*, *y* and *z*; $\Delta X/c = 1.5$

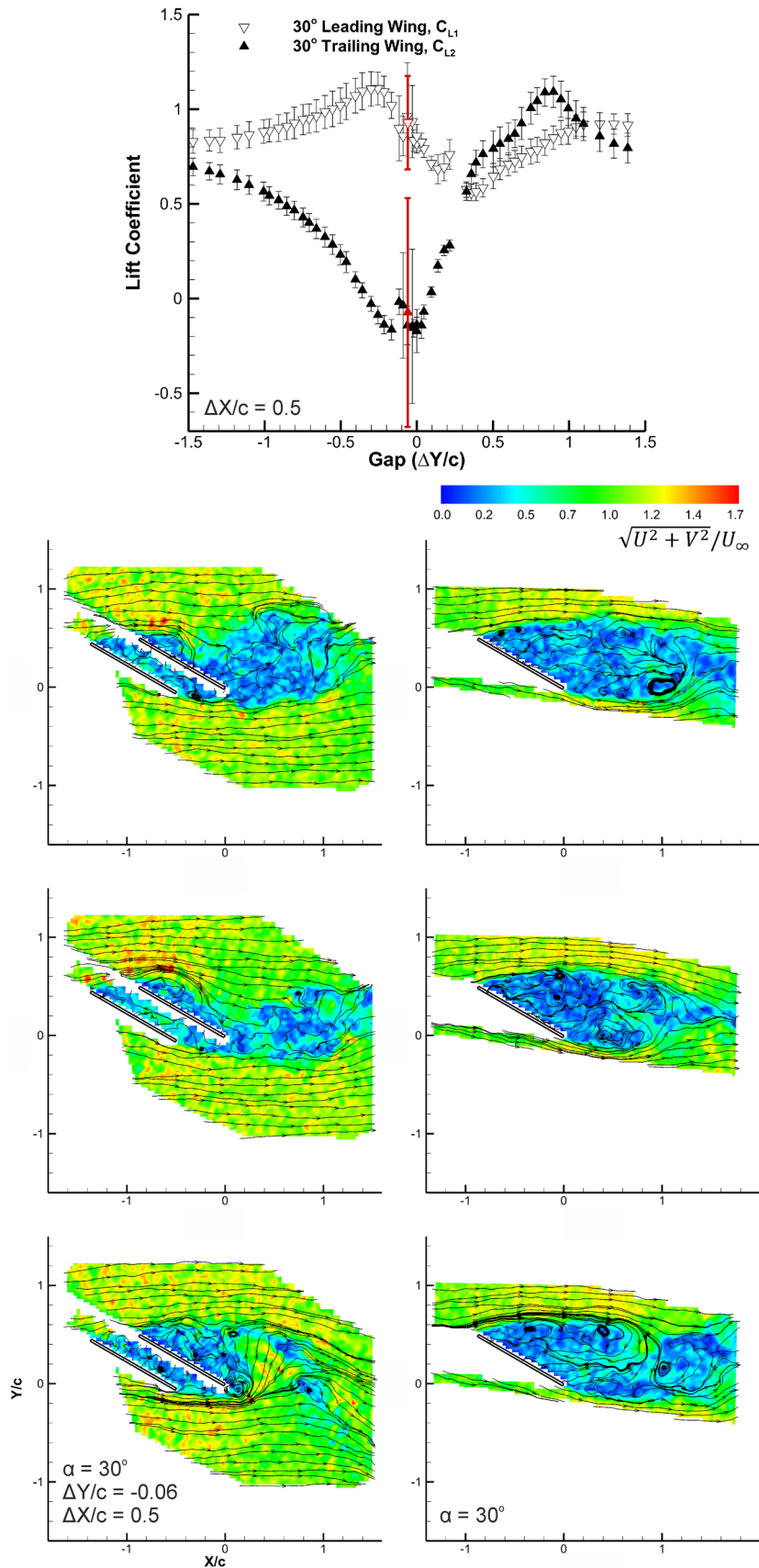
leading and trailing wing lift coefficient is observed. Instantaneous velocity magnitude fields presented in Fig. 22 show that the shear layer emanating from the leading edge of the leading wing consistently remains detached and does not reattach to the upper surface of the trailing wing. The unsteadiness in this case is likely due to the fluctuating state of the wing wakes. Flow passing underneath the leading wing is observed to alternate between passing between and underneath the two wings. The effect results in the wing wakes alternating between unified and separate states which not only provides insight into the cause of the

unsteady forces, but also indicates a plausible explanation as to the large unified region of flow velocity SD discussed in Fig. 20. This second unsteady flow is therefore characterized by switching of the inter-wing flow between merged and separate wakes (switching between IF3 and MW2).

4 Conclusions

Experiments were performed to investigate aerodynamics of two-wing configurations at a low Reynolds number

Fig. 21 Lift coefficients for wings in tandem ($\Delta X/c = 0.5$) at 30° angle of attack (top). Standard deviation of the lift coefficient is indicated by bars. Instantaneous PIV images are presented in the form of normalized velocity magnitude for a gap of $\Delta Y/c = -0.06$ which exhibited the greatest standard deviation of lift (left). Single-wing instantaneous flow fields at 30° are presented (right) for comparison



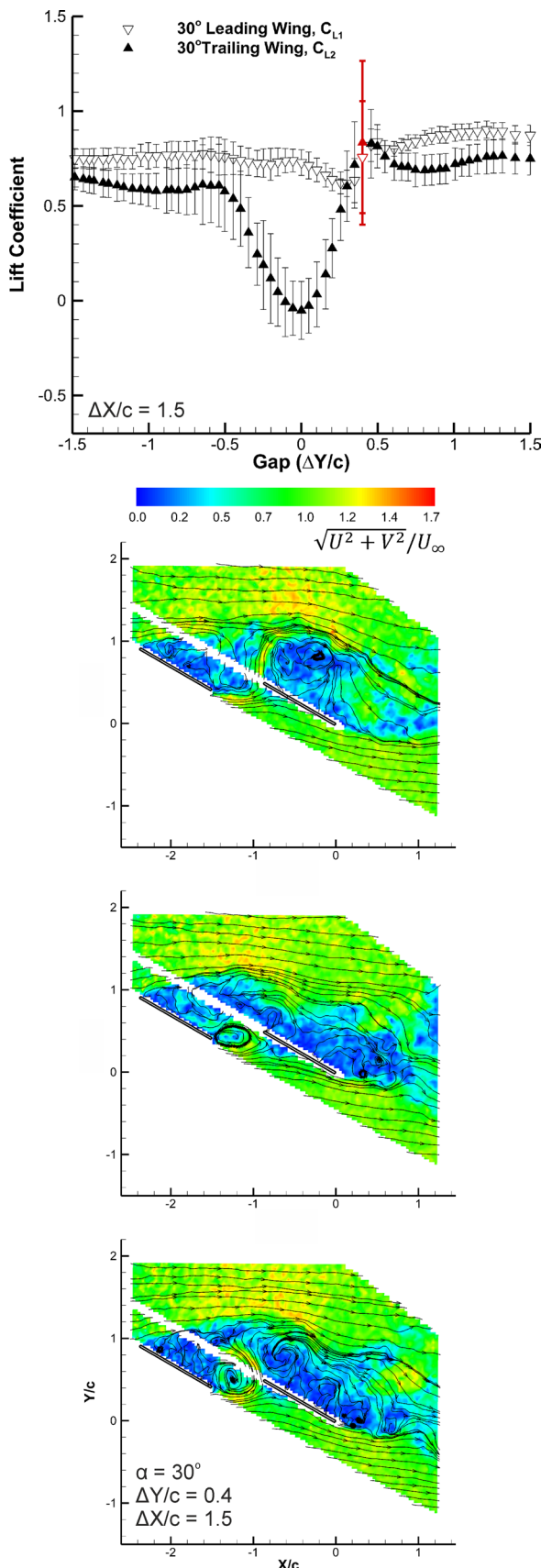


Fig. 22 Lift coefficients for wings in tandem ($\Delta X/c = 1.5$) at 30° angle of attack (top). Standard deviation of the lift coefficient is indicated by bars. Instantaneous PIV images are presented in the form of normalized velocity magnitude for a gap of $\Delta Y/c = 0.4$ which exhibited the greatest standard deviation of lift (bottom)

of 100,000 for a range of values of stagger and gap. These measurements have shown that two-wing configurations are a viable method of overcoming the challenges of low Reynolds number flight. Lift increases, and stall angle is delayed significantly for certain configurations. Aerodynamic benefits are observed in the post-stall regime of the single wing. Hence, the use of two-wing configurations can be considered as a passive flow control method. The maximum total lift ratio exceeded $R_L = 1.3$ at high angles of attack $\alpha = 25^\circ$ and 30° for $\Delta X/c = 0.5$. The maximum aerodynamic efficiency was found to increase at high angles of attack as $\Delta X/c$ increases. The greatest improvement was noted to occur for $\Delta X/c = 1.5$, $\Delta Y/c = 0.3$ and $\alpha = 20^\circ$ yielding $R_{AE} = 1.07 \pm 0.04$ and was associated with IF3. The best performance in terms of power efficiency occurred when $\Delta X/c = 0.5$, $\Delta Y/c = 0.85$ and $\sigma = 25^\circ$ resulting in a 20 % increase compared with the single wing and was associated with a high-speed inter-wing flow aft of the leading wing's lower surface termed IF2.

PIV measurements of selected configurations exhibiting interesting force coefficient properties revealed five critical types of flow field: (1) high-speed inter-wing flow interacting with both wings resulting in low lift due to the high-speed flow on the upper wing's lower surface, termed IF1; (2) high-speed inter-wing flow aft of the leading wing's lower surface termed IF2, associated with high lift; (3) partially divided wakes with a discreet amount of inter-wing flow termed IF3, which was associated with a merged region of high flow unsteadiness in the vicinity of the leading wing's upper surface; (4) tandem wing flow in which the wing's wakes are merged due to the aft wing residing in the fore wing's wake termed MW1, which was also associated with high unsteadiness; (5) merged wakes with both wing's lower surfaces being subject to the freestream termed MW2. Hence, interaction of separated shear layers from the leading wing with the trailing wing determines the aerodynamics of the two-wing configurations at high angles of attack. The type of interaction determines which wing has larger lift. We believe that these observations for massively separated flows for thin flat-plate wings will be similar for different airfoil shapes.

The two-wing configurations do not necessarily have much larger lift fluctuations than the single flat-plate wing at the same angle of attack, except for particular configurations. The flow type MW1 was found to exhibit a surge in unsteady forces around values of $\Delta X/c = 0.5$,

$\Delta Y/c = -0.06$ and $\alpha = 30^\circ$ which was attributed to a switching between stalled and unstalled states over the trailing wing's upper surface similar to the phenomenon reported by Zaman et al. (1989) for single wing. A surge in unsteady forces was also found to occur for the IF3 flow type at distinct values of $\Delta X/c = 1.5$, $\Delta Y/c = 0.4$ and $\alpha = 30^\circ$. This effect was attributed to a switching between flow types IF3 and MW2, i.e., a switching between merged and distinct wakes.

Acknowledgments This work was supported by the University of Bath University Research Scholarship. The authors would also like to acknowledge the University of Bath's technical staff for their continued support. The authors also thank the EPSRC Engineering Instrument Pool.

References

- Carmichael B (1981) Low Reynolds number airfoil survey. vol 1. NASA CR 165803, Hampton, VA
- Cleaver DJ, Wang Z, Gursul I, Visbal M (2011) Lift enhancement by means of small-amplitude airfoil oscillations at low Reynolds numbers. *AIAA J* 49:2018–2033. doi:[10.2514/1.J051014](https://doi.org/10.2514/1.J051014)
- Davis WR, Kosicki BB, Boroson DM, Kostishack DF (1996) Micro air vehicles for optical surveillance. *Linc Lab J* 9:197–214
- Frampton KD, Goldfarb M, Monopoli D, Cveticanin D (2001) Passive aeroelastic tailoring for optimal flapping wings. In: Mueller TJ (ed) Fixed and flapping wing aerodynamics for micro air vehicle applications. Progress in Astronautics and Aeronautics, AIAA, Reston, pp 473–482
- Glauert H (1959) Elements of aerofoil and airscrew theory. Cambridge University Press, Cambridge
- Jones R, Cleaver DJ, Gursul I (2015) Fluid-structure interactions for flexible and rigid tandem-wings at low Reynolds numbers. 53rd AIAA Aerospace Sciences Meeting, Kissimmee, FL, AIAA Paper-2015-1752
- Knight M, Noyes R (1929a) Wind tunnel pressure distribution tests on a series of biplane wing models part I : effects of changes in stagger and gap. NACA TN 310
- Knight M, Noyes R (1929b) Wind tunnel pressure distribution tests on a series of biplane wing models part II : effects of changes in decalage, dihedral, sweepback and overhang. NACA TN 325
- Knight M, Noyes R (1929c) Wind tunnel pressure distribution tests on a series of biplane wing models part III : effect of changes in various combinations of stagger, gap, sweepback and decalage. NACA TN 330
- Moffat RJ (1985) Using uncertainty analysis in the planning of an experiment. *J Fluid Eng* 107:173–178. doi:[10.1115/1.3242452](https://doi.org/10.1115/1.3242452)
- Moschetta J-M, Thipyopas C (2007) Aerodynamic performance of a biplane micro air vehicle. *J Aircr* 44:291–299. doi:[10.2514/1.23286](https://doi.org/10.2514/1.23286)
- Mueller TJ (2000) Aerodynamic measurements at low Reynolds numbers for fixed wing micro-air vehicles. RTO AVT/WKI, Special Course on Development and Operation of UAVs for Military and Civil Applications, von Karman Institute, September, RTO-EN-9, ISBN 92-837-1033-9
- Mueller T, DeLaurier JD (2001) An overview of micro air vehicle aerodynamics. In: Mueller TJ (ed) Fixed and flapping wing aerodynamics for micro air vehicle applications. Progress in Astronautics and Aeronautics, AIAA, Reston, pp 1–10
- Mueller TJ, DeLaurier JD (2003) Aerodynamics of small vehicles. *Annu Rev Fluid Mech* 35:89–111. doi:[10.1146/annurev.fluid.35.101101.161102](https://doi.org/10.1146/annurev.fluid.35.101101.161102)
- Null W, Shkarayev S (2005) Effect of camber on the aerodynamics of adaptive-wing micro air vehicles. *J Aircr* 42:1537–1542
- Olson EC, Selberg B (1976) Experimental determination of improved aerodynamic characteristics utilizing biplane wing configurations. *J Aircr* 13:256–261. doi:[10.2514/3.44523](https://doi.org/10.2514/3.44523)
- Pelletier A, Mueller TJ (2000) Low Reynolds number aerodynamics of low-aspect-ratio, thin/flat/cambered-plate wings. *J Aircr* 37:825–832. doi:[10.2514/2.2676](https://doi.org/10.2514/2.2676)
- Prandtl L, Tietjens O (1957) Applied hydro-and aeromechanics. Dover Publications, Inc., Dover, pp 211–212
- Scharpf DF, Mueller TJ (1992) Experimental study of a low Reynolds number tandem airfoil configuration. *J Aircr* 29:231–236. doi:[10.2514/3.46149](https://doi.org/10.2514/3.46149)
- Selig MS, Donovan JF, Fraser DB (1989) Airfoils at low speeds. H.A. Stokely, Virginia Beach
- Torres G, Mueller TJ (2000) Micro aerial vehicle development: design, components, fabrication, and flight-testing. In: AUVSI Unmanned Systems 2000 Symposium and Exhibition, pp. 11–13
- Traub LW (2001) Theoretical and experimental investigation of biplane delta wings. *J Aircr* 38:536–546. doi:[10.2514/2.2794](https://doi.org/10.2514/2.2794)
- Wang Z, Gursul I (2012) Unsteady characteristics of inlet vortices. *Exp Fluids* 53:1015–1032. doi:[10.1007/s00348-012-1340-2](https://doi.org/10.1007/s00348-012-1340-2)
- Zaman K, McKinzie D, Rumsey C (1989) A natural low-frequency oscillation of the flow over an airfoil near stalling conditions. *J Fluid Mech* 202:403–442. doi:[10.1017/S0022112089001230](https://doi.org/10.1017/S0022112089001230)